

**RACORO Continental Boundary Layer Cloud Investigations. Part III: Separation of
Parameterization Biases in Single-Column Model CAM5 Simulations of Shallow Cumulus**

Wuyin Lin¹, Yangang Liu¹, Andrew M. Vogelmann¹, Ann Fridlind², Satoshi Endo¹, Hua Song¹,

Sha Feng^{3,4}, Tami Toto¹, Zhijin Li^{3,4} and Minghua Zhang⁵

1. Brookhaven National Laboratory

2. NASA Goddard Institute for Space Studies

3. UCLA Joint Institute for Regional Earth System Science and Engineering (JIFRESSE)

4. Jet Propulsion Laboratory and JIFRESSE

5. Stony Brook University

Accepted for publication in
Journal of Geophysical Research Atmospheres
April 2015

Corresponding Author Address:

Dr. Wuyin Lin
Biological, Environmental & Climate Sciences Department
Brookhaven National Laboratory
75 Rutherford Drive
Upton, NY 11973 Phone: (631)3447249
Email: wlin@bnl.gov

Abstract

Climatically important low-level clouds are commonly misrepresented in climate models. The FAsT-physics System TEStbed and Research (FASTER) project has constructed case studies from the Atmospheric Radiation Measurement (ARM) Climate Research Facility's Southern Great Plain site during the RACORO aircraft campaign to facilitate research on model representation of boundary-layer clouds. This paper focuses on using the single-column Community Atmosphere Model version 5 (SCAM5) simulations of a multi-day continental shallow cumulus case to identify specific parameterization causes of low-cloud biases. Consistent model biases among the simulations driven by a set of alternative forcings suggest that uncertainty in the forcing plays only a relatively minor role. In-depth analysis reveals that the model's shallow cumulus convection scheme tends to significantly under-produce clouds during the times when shallow cumuli exist in the observations, while the deep convective and stratiform cloud schemes significantly over-produce low-level clouds throughout the day. The links between model biases and the underlying assumptions of the shallow cumulus scheme are further diagnosed with the aid of large-eddy simulations and aircraft measurements, and by suppressing the triggering of the deep convection scheme. It is found that the weak boundary layer turbulence simulated is directly responsible for the weak cumulus activity and the simulated boundary layer stratiform clouds. Increased vertical and temporal resolutions are shown to lead to stronger boundary layer turbulence and reduction of low-cloud biases.

1. Introduction

Differences in the response of low clouds to climate change scenarios are well recognized as being responsible for most of the spread in model-based estimates of equilibrium climate

47 sensitivity and transient climate response [*Randall et al.*, 2007; *Dufresne and Bony*, 2008;
48 *Boucher et al.*, 2013]. This problem has recently been traced to atmospheric convective mixing
49 between the lower and middle troposphere [*Sherwood et al.*, 2014], in that model climate
50 sensitivities are found to be closely related to the strength of parameterized small-scale mixing.
51 Shallow cumuli serve as a critical link in this mixing process, and numerical experiments have
52 found that they contribute significantly to the spread in climate sensitivity [*Medeiros et al.*,
53 2008; *Gettelman et al.*, 2012; *Zhang et al.*, 2013].

54 Aside from the role in model estimate of climate sensitivity, the importance of shallow
55 cumulus processes is manifold. For example, shallow cumuli can have a strong impact on the
56 Earth's net radiation budget [*Hartmann et al.*, 1992]. Close coupling of shallow cumulus with
57 boundary layer turbulence can intensify surface and boundary layer turbulent transport.
58 Thereby this coupling plays an important role in maintaining the energy and moisture budget of
59 the lower troposphere, and in determining the vertical thermodynamic structure of the
60 boundary layer and free troposphere [Siebesma 1998]. Latent heating associated with shallow
61 cumulus activity also plays a crucial role in driving low-level convergence to fuel deep
62 convection in the tropics [e.g., *Wu et al.*, 2003]. Proper transition from shallow cumulus to deep
63 convection, therefore, is critical at multiple time scales, from the diurnal cycle of summer time
64 continental precipitating convection [*Del Genio and Wu*, 2010; *Zhang and Klein*, 2010], to the
65 phase and propagation of intra-seasonal oscillation in the tropics [*Benedict and Randall*, 2007;
66 *Del Genio et al.*, 2012].

67 Representation of shallow cumulus convection, therefore, can have a large impact on the
68 performance of numerical weather-prediction and climate models [e.g., *Tiedtke et al.*, 1988].

69 Separate treatments of shallow and deep convection are commonly used in major weather and
70 climate models, for example, the European Centre for Medium Range Forecast (ECMWF)'s
71 Integrated Forecasting System (IFS) [*Bechtold et al.*, 2004], the National Center for Atmospheric
72 Research (NCAR) Community Atmosphere Model (CAM) [*Neale et al.*, 2010; *Neale et al.*, 2012],
73 the Geophysical Fluid Dynamics Laboratory (GFDL)'s Atmosphere Model (AM) [*Donner et al.*,
74 2011], and the Met Office's Unified Model (UM) [*Walters et al.*, 2011]. Vertical eddy fluxes of
75 energy and moisture comprise air motions spanning multiple scales, and hence separate
76 parameterizations for different characteristic scales can be justifiable in modeling
77 implementation. The shallow cumulus parameterization problem may become even more
78 outstanding when climate models approach cloud-resolving resolution and no longer need to
79 parameterize deep convection, because the small-scale processes involving shallow cumuli and
80 their interaction with boundary layer turbulence will still critically rely on parameterized
81 representation. In recent years, developments have aimed at close coupling of shallow cumulus
82 and moist turbulence parameterizations [e.g., *Park and Bretherton*, 2009], unified treatments
83 [e.g., *Larson and Golaz*, 2005; *Bogenschutz et al.*, 2012; *Siebesma et al.*, 2007; *Suselj et al.*,
84 2012], or incorporation of high-order turbulence closure into superparameterized modeling
85 framework [*Bogenschutz and Krueger*, 2013; *Cheng and Xu*, 2013; *Xu and Cheng*, 2013]. Each of
86 these developments has led to improved simulations of low-level clouds, particularly in the
87 transition from stratocumulus to cumulus regime in the marine environment. Despite such
88 promising advancements, simulation of low-level clouds in climate models continues to be
89 challenging because of the fine-scale characteristic of the related processes. Shallow cumulus
90 clouds are ubiquitous over ocean and land and can occur under various environmental

conditions [Warren *et al.*, 1986; Warren *et al.*, 1988; Norris, 1998; Johnson *et al.*, 1999; Zhu and Albrecht, 2002; Berg and Kassianov, 2008]. Therefore, it is important to rigorously test and evaluate new parameterizations over each representative regime, ideally with high-quality in-situ measurements, to steadily narrow climate projection uncertainty.

This paper focuses on evaluating the performance of the CAM5 University of Washington shallow convection scheme (hereafter UWshcu) [Bretherton *et al.*, 2004; Park and Bretherton, 2009] in simulating continental fair weather cumuli. This is part III in a series of modeling studies of continental boundary layer cloud processes that use case studies based on the RACORO field campaign. Part I details the case generation and the ensemble large-scale forcings that are assembled for modeling studies [Vogelmann *et al.*, 2015]. Part II uses large-eddy simulations and in-situ cloud microphysics observations to study the shallow cumulus case [Endo *et al.*, 2015].

The shallow cumulus case studies (see companion paper Vogelmann *et al.* [2015]) are constructed based on measurements from the Atmospheric Radiation Measurement (ARM) [Stokes and Schwartz, 1994; Ackerman and Stokes, 2003; Mather and Voyles, 2013] Climate Research Facility's Southern Great Plain site, and from the 2009 RACORO (Routine ARM Aerial Facility (AAF) Clouds with Low Optical Water Depth (CLOWD) Optical Radiative Observations) aircraft campaign that aims to facilitate research on model representation of boundary layer clouds [Vogelmann *et al.*, 2012]. Unlike many other shallow cumulus cases, which focus on the steady state marine environments, the RACORO cases emphasize time-varying environmental conditions and are able to capitalize on high-quality ground-based and in-situ aircraft measurements. Compared to simulations of quasi-steady idealized cases, simulations of

transient cases have more freedom to evolve and behave more similarly to free model runs in terms of how physical processes interact with each other and how they respond to time-varying environment, perhaps especially during regime transitions.

The paper is organized as follows. Section 2 describes the model and data used. Section 3 shows the results of SCAM5 simulation of a multi-day shallow cumulus case, followed by the investigation of SCAM5 behavior in section 4. A summary and discussion are presented in section 5.

2. Model and data descriptions

2.1. Model

This study uses the single-column mode of the Community Atmosphere Model (CAM) version 5 (CAM5) which is the atmosphere model component of the Community Earth System Model (CESM) [Neale *et al.*, 2012]. With the large-scale dynamics prescribed from carefully designed case studies, the single-column model framework enables focusing on the model physics.

The physical parameterizations in CAM5 include the University of Washington moist turbulence parameterization [Bretherton and Park, 2009], a two-moment scheme for cloud microphysics [Morrison and Gettelman, 2008], the Rapid Radiative Transfer Model (RRTM) for longwave and shortwave radiative transfer [Iacono *et al.*, 2008], a cloud macrophysics scheme [Park *et al.*, 2014], a deep convection scheme [Zhang and McFarlane, 1995; Neale *et al.*, 2008], and the University of Washington shallow cumulus scheme [Bretherton *et al.*, 2004; Park and

Bretherton, 2009]. Because the primary objective of this work is to investigate the simulation of shallow cumulus in the CAM5 model, the UWshcu scheme is detailed below.

The UWshcu scheme is based on a single entrainment-detrainment buoyancy-sorting plume model. The closure for cloud-base mass flux and updraft velocity uses convective inhibition (CIN) and boundary layer turbulence kinetic energy (TKE). The scheme diagnoses the bulk vertical velocity in cumulus updrafts, allowing a more complete representation of aerosol activation and cloud microphysical evolution. This scheme has been adopted in GFDL (*Donner et al.*, 2011] and CAM5 [*Neale et al.*, 2012] models. The implementation in the CAM5, coupled with the University of Washington moist turbulence scheme [*Bretherton and Park*, 2009], has led to improved simulations in many aspects [*Park and Bretherton*, 2009], particularly in thermodynamic structure and cloud radiative forcing in both single-column model (SCM) and global model settings. The adoption of the UWshcu scheme also led to the largest mid-latitude feedback difference and largest change in climate sensitivity compared to the previous version of CAM [*Gettelman et al.*, 2012; *Kay et al.*, 2012]. Given the popularity of CAM in the climate modeling community and the significance of the UWshcu scheme in CAM simulations, it is valuable to assess the performance of the scheme under realistic atmospheric conditions in order to better understand its behavior in idealized or climatological settings.

2.2. Large-scale forcing and cloud data

A suite of different measurements collected with different platforms/instruments are used in the model evaluation and analysis. This sub-section briefly describes the key data sets.

Long-term (1999-2010) ARM continuous forcing data [Xie *et al.*, 2004] over the SGP are first used to drive the SCAM5 to reveal systematic model biases in simulating continental boundary layer clouds, which will be further examined using the RACORO shallow cumulus case study (May 22 – 25, 2009). The long-term simulation follows the setup as described in Song *et al.* [2013], which is typical for cloud modeling in single-column mode.

For the RACORO case study, the SCAM5 simulations are driven by hourly large-scale forcings from three independent data sources: the operational ARM continuous forcing [Xie *et al.*, 2004], derived forcings from ECMWF operational short-term forecasts, and derived forcings from a cloud-resolving multi-scale data assimilation (hereafter MS-DA; Li *et al.* [2015]). Each data set has a pair of forcings corresponding to the ARM standard domain (300 km) and a reduced domain (150 km). The ARM continuous forcing for the standard domain with 25-hPa vertical resolution is an operational product, and the reduced domain forcing with 10-hPa resolution is specially produced for this case study. The ECMWF forcing data are derived from ECMWF 12-36 hour forecasts. Other than the standard state variables, the forecast data archived at the ARM External Data Center also record hourly surface fluxes and necessary fields for deriving large-scale advective tendencies of temperature and moisture. The quantities needed for the SCAM5 simulations are assembled from a series of daily reinitialized forecasts into a format consistent with the ARM continuous forcing. The unique advantage of this Numerical Weather Prediction (NWP) model-based forcing is that the atmospheric state and large-scale forcings are from the same full dynamical model and, hence, inherit strict internal dynamical consistency. The MS-DA forcing data are derived from a multiple-scale data assimilation system that employs an innovative decomposition of data assimilation at multiple scales and can explicitly

resolve clouds and other dynamical and physical processes down to a 2-km resolution (see *Li. et al.* [2015] and *Feng et al.* [2015a, b] in this special issue for more details). Interested readers can refer to *Vogelmann et al.* [2015] for more details on the ensemble forcing data and their use for simulations.

Because the observations (i.e., ARM ground-base cloud measurement) used for evaluation are of clouds passing over the SGP Central Facility, the central facility sounding profiles of temperature and moisture at 11:30 AM UTC (5:30 AM local time) are used to initialize the model to provide the best correspondence with the observed cloud state. The LES simulations from *Endo et al.* [2015] used in this paper are initialized the same way. Each RACORO case simulation is run for 60 hours and, at each time step, the model temperature and humidity profiles are relaxed toward the time varying observed profile with a 12-hour time scale.

ARM's Active Remote Sensing of Clouds (ARSCL; *Clothiaux et al.* [2000]) value-added cloud boundary product is used as the observational reference for the long-term simulations and the RACORO case study. The ARM Climate Research Facility baseline cloud microphysical property product (MICROBASE; *Dunn et al.* [2011]) together with the ARM continuous forcing data [*Xie et al.*, 2004] are further used to characterize cloud types following the ISCCP algorithm [*Rossow et al.*, 1996; *Klein and Jakob*, 1999]. Cloud types are determined by using 10-second MICROBASE cloud property profiles to feed the ISCCP simulator [*Klein and Jakob*, 1999] from the Cloud Feedback Model Intercomparison Project (CFMIP) Observational Simulator Package (COSP), with thermodynamic profiles specified by the nearest hourly values from the ARM continuous forcing data. The 10-second cloud types along with their hourly occurrence are aggregated into

the hourly ISCCP histogram. The cloud type characterization is used to aid in the sampling of prevailing low-level cloudy conditions that are not obscured by overlying higher-level clouds, in order to establish a climatology of low-level clouds represented by the RACORO case study.

3. Results

3.1 Long-term SCAM5 simulations and a low-level cloud climatology

The primary focus of this section is to examine how well physical parameterizations in CAM5 reproduce continental low-level clouds, especially those that are weakly forced.

The ISCCP cloud classifications are employed to identify low-level clouds that are not strongly associated with synoptic events or warm season precipitating deep convective cloud systems. In the ISCCP classification, observed and model-simulated clouds are classified according to cloud-top height and cloud optical thickness, where low cloud refers to clouds with a top-height below 680 hPa and middle- and high-level clouds are above this level. The low-level cloud climatology generated from observations and simulations includes only those conditions with hourly mean sky coverage of middle and high-level clouds combined being less than 10%.

Figure 1a shows the 1999-2010 mean seasonal variation of the observed and SCAM5-simulated frequency of low-level cloud occurrence, calculated as the ratio of the number of qualified low-level cloudy conditions to the total number of hourly points during the period. The model frequency is many times greater than observed throughout the year, and the discrepancy is greatest during the warm season. In contrast, the simulated mean low-level cloud amounts sampled for all qualified low-level cloudy conditions are lower than the

observed (Figure 1b). The discrepancy in occurrence frequency dominates the biases, leading to an overestimation of low-level cloud amount (which equates to the product of Figures 1a and 1b, not shown) even during the warm season. We note that, during the warm seasons, the combined mean occurrence frequency of middle and high-level clouds exceeding 10% in the SCAM5 is within 5% of the MICROBASE values (not shown).

Figure 2 further shows the occurrence frequency of each ISCCP-defined cloud type during the warm season from the observations and the SCAM5 simulations. The higher occurrence frequency in SCAM5 is predominantly from clouds with low cloud tops (below 800 hPa) and intermediate optical thicknesses. Thin (optical depth < 3.6) and thick (optical depth > 23) clouds also occur more frequently in the model. It is clear that low-level clouds in the observations are situated at higher altitudes and/or with cloud tops penetrating deeper, as most of the clouds have tops above 800 hPa. It can also be seen that low clouds in the model are slightly more influenced by deep convective activity, as indicated by the noticeable presence of optically thick, high-top clouds. As will be seen in the next section, this is related to more frequent triggering of spurious deep convection in the model in early afternoon during the warm season. Although the bias in mean cloud amount of all low-level cloudy scenes in the warm season is small (Figure 1b), the cloud properties in terms of cloud-top height and cloud optical thickness still exhibit significant differences. The most obvious difference, as shown in Figure 3, is that the model low-level clouds have lower cloud-top height and are mostly optically thinner. Given that the SCAM5 simulations are largely constrained by observational surface fluxes and advective forcing, this result indicates that model clouds are not sufficiently developed at the times when the observed clouds are typically present. In compensation, the model produces other cloud

types that are not present in the observations, leading to excessive low-level cloud occurrence in the model.

3.2 Investigation using a RACORO case study

As seen in the previous section, the model biases are most pronounced during the warm season, in terms of the frequency of low-level cloud occurrence and cloud types. In this section, we use a warm-season, multiple-day shallow cumulus cloud case study developed from the RACORO field campaign to investigate how the model biases can be traced to deficiencies in model physics and how biases in the production of one cloud type can lead to excessive amounts of other cloud types on a daily time scale.

3.2.1. SCAM5 simulations driven by operational ARM forcings

The case was developed to study processes that influence the formation and evolution of continental low-level clouds, and to investigate model performance in reproducing such clouds. Unlike model approaches that use steady-state low-level clouds, the RACORO case enables study of the development and transitions of boundary layer and cloud states within a realistically transient atmospheric environment. While the physical processes responsible for the evolution of the boundary layer and clouds operate at fine spatial and temporal scales that require large-eddy simulation models to resolve (e.g., *Endo et al.* [2015] and *Vogelmann et al.* [2015] in this special issue), the assessment of physical parameterizations used in climate models can be tested in a single-column model setting [e.g., *Randall et al.*, 1996; *Kennedy et al.*, 2010; *Song et al.*, 2013], including those that focus on continental shallow cumulus [e.g., *Lenderink et al.*, 2004; *Neggers et al.*, 2004]. Here the RACORO shallow cumulus case is used to

assess the performance in the SCAM5 of the physical parameterizations that contribute to low-level cloud production.

For the RACORO shallow cumulus case study period, the large-scale advective forcing is weak and the cumulus convection is primarily driven by surface fluxes that peak around noontime. In observations (Figure 4a), cumulus clouds start to develop in the morning and dissipate in the mid-afternoon, which is consistent with the typical life cycle of continental shallow cumulus clouds [*e.g.*, *Zhu and Albrecht*, 2003]. The cloud-base height increases during the daytime and cloud-top penetrates up to 4 km. The structures of the cumulus clouds are similar for each day in the three-day period and there are few overlying higher-level clouds. The cumulus cloud amount developed due to surface fluxes is generally less than 30%, except for the greater amount before 9 AM local time on the first day that is within the residual layer of the previous day (see discussion in *Vogelmann et al.* [2015]). It is also clear from observations that the cumulus completely dissipate by the end of each day, leaving no cloud remnants in the evening hours. The daily evolution of the cumulus two to three hours before and after noontime is remarkably similar, especially for the second and third days.

The time-height variation of cloud fraction simulated by the SCAM5 driven by the standard ARM continuous forcing is shown in Figure 4b. The model configuration includes all of the standard CAM5 physics for this simulation. The most outstanding bias occurs from near noon to late afternoon when the model clouds penetrate as high as 7 km, far deeper than the observed cloud-top height seen in Figure 4a. This bias is associated with deep convection that is triggered when convective available potential energy (CAPE) exceeds a threshold value. Such over-

triggering of deep convection that follows the solar diurnal cycle has been well documented [e.g., *Xie and Zhang, 2000; Guichard et al., 2004; Song et al., 2014*] The prematurely triggering and over-deepening of convective clouds make the deep scheme unsuitable for modeling fair weather shallow cumulus. Another outstanding bias is the persistence of nighttime clouds that are not present in the observations. Similar problem has also been reported in other SCM simulations of warm season continental low-level clouds [e.g., *Guichard et al., 2004; Lenderink et al., 2004*]. Even the global model CAM5 simulation with fully interactive dynamics using the Cloud Associated Parameterization Testbed (CAPT) framework (using simulations from *Xie et al. [2012]*) produces remarkably similar cloud biases over the SGP during the RACORO period (not shown). The model biases can be attributed to inaccurate representations of physical processes and/or to the forcing data used to drive the simulations. The focus of this work is to investigate the causes due to imperfect physical representation of the related processes, but it is necessary to first ensure that uncertainties associated with the forcing data are not the primary culprit.

3.2.2. SCAM5 sensitivity to large-scale forcing

To evaluate how uncertainty in large-scale forcing may impact the simulations, three independent forcing data sets are used to drive the model using both standard and reduced domain sizes. The involvement of the reduced domain forcing is meaningful considering that the shallow cumulus clouds of interest are small scale in nature and, for this case, are a localized phenomenon.

The simulated time-height cloud variation using the alternative forcing data is shown in Figures 4c – g. The outstanding biases seen in Figure 4b with the standard ARM forcing mostly

also appear in these simulations, though the biases are slightly moderated in some cases. The simulation using the ARM reduced-domain forcing has slightly less spurious deep convection for days 2 and 3, and there is a break in the persistency of the nighttime low-level clouds during the late night to early morning hours of day 2. Simulations using the ECMWF forcings also yield less spurious deep convection, and the penetration depth is shallower when triggered. Similar to the contrast between the two ARM simulations, the spurious deep convection is less pervasive with the ECMWF forcing for the reduced domain. However, the bias in the persistency of nighttime clouds has a somewhat different relation with the convective activity earlier in the day. It appears that for the simulation with more active afternoon convection (Figures 4d and 4e between days 1 and 2, and between days 2 and 3), the ensuing low level clouds are more stable. This to some degree is opposite to what can be seen in Figures 4b and 4c between days 1 and 2, but similar between days 2 and 3. The simulations driven by MS-DA forcings exhibit more distinguishable differences from the other simulations, although they are also plagued by spurious deep convection and have excessive low-level clouds in comparison to observations. The afternoon deep convection penetrates higher than the simulations by other forcings, and nighttime-to-early-morning low-level clouds are closer to the surface. The relationship between afternoon deep convective activity and the ensuing nighttime buildup of low-level clouds bears some similarity to that seen in the two ECMWF simulations. This is not as true for the simulations with the ARM forcings. By construction the non-ARM-based forcings are considered to have better consistency in their internal dynamics because they involve complete dynamical models. However, there is insufficient evidence to suggest that the

presumed dynamical consistency of the forcing data can explain the different relationships noted above.

3.2.3. Pinpointing the causes for biases

A number of factors (e.g., deficiencies associated with deep and shallow convection schemes) may be related to the model biases identified above. The following experiments and diagnosis are designed to pinpoint the specific parameterized processes associated with these biases.

It is obvious from Figure 4 that over-triggering of deep convection causes large biases in the simulated cloud field when the standard model configuration is used. Since shallow cumulus appears in the observations at the times when deep convection tends to be triggered in the model, the deep convection scheme is turned off in the next set of simulations to focus on the processes more relevant to boundary layer clouds. As shown in Figure 5, when the deep convection is turned off, the model clouds are indeed confined to the lower levels. (Note that in this and the following figures the extent of the vertical coordinate is reduced to focus on the lower levels.) However, other biases seen in the standard simulation remain, particularly the persistence of low-level clouds throughout the night.

After removing the biases due to the deep convective scheme, two parameterized processes that remain to directly contribute to cloud production are the shallow cumulus scheme and the relative humidity-based stratiform cloud scheme. The cloud amounts produced directly by the shallow cumulus scheme are shown in Figure 6. The shallow cumulus cloud production is mainly from late morning to early afternoon, as expected for typical fair weather cumulus. The timing

of the shallow cumulus activity is in reasonable agreement with the observations for each of the three days, which suggests the shallow cumulus scheme and its coupling with boundary-layer moist turbulence scheme respond fairly well to the prescribed environmental conditions. Also in agreement with the observations, the simulated shallow cumulus cloud-base height increases as the day progresses. These consistencies appear in all of the simulations with the different forcings. However, the cumulus cloud amounts are less than half of the observed cloud amount shown in Figure 4a and the vertical extent of the simulated cumulus is also mostly smaller. As the total cloud amount in the model in Figure 5 is the sum from the cumulus and stratiform cloud schemes, clearly the night time low-level clouds are entirely from the stratiform scheme. Furthermore, even when shallow cumulus convection is active, stratiform cloud production still contributes a significant fraction to the total clouds. Although the addition of stratiform cloud helps bring the total cloud amount into better agreement with observations during the shallow convection events, the inaccurate physical representation is expected to result in unfavorable boundary layer and cloud development.

The lesser cumulus cloud production seen in Figure 6 suggests that the shallow cumulus activity is weaker in the model. The surface turbulence fluxes supply plenty of moisture to the boundary layer (given Figure 5), but the weaker cumulus convection and suppression of cumulus updraft penetration does not sufficiently ventilate the abundance of moisture to the free troposphere. The resulting moisture buildup in the boundary layer can be seen in Figure 7, which shows a layer between 1.5 km and 2 km with much higher relative humidity in SCAM5 simulations than in the observations. Both model simulations lack upward moistening of the free troposphere. The simulation with deep convection has deeper penetration of moist air

compared to the one without deep convection. Still, the aggregated convective moisture transport due to the deep and shallow schemes appears to be less than the observed. This moisture buildup will not only promote stratiform cloud production during active convective periods, often at lower altitudes, but the moister boundary layer also favors the stratiform cloud production during nighttime when temperature drops and surface-driven turbulence subsides. Consequently, errors originating from insufficient cumulus ventilation go well beyond the active cumulus period and lead to lasting distortions in the boundary layer structure and the associated low-level clouds. The excessive stratiform cloud production can be clearly seen by contrasting Figures 5 and 6, which exclude the large error source induced by deep convection. Below, we further investigate the factors that may be responsible for the weaker shallow cumulus activity in the model, with the aid of flight measurements and LES simulations for this cumulus case.

4. Investigation of shallow cumulus convection using an integrated SCM-LES framework

In this section, we assess the modeled shallow cumulus activity and factors that are closely related to how the cumulus activity is parameterized, including cumulus mass flux, planetary boundary layer (PBL) turbulent kinetic energy (TKE), and entrainment and detrainment profiles in the cumulus layer. The primary references for the assessment are two LES model simulations. Aircraft measurements, when available, are also used to derive properties that can be related to the turbulence and convective activity.

Without losing generality, we focus on the SCAM5 simulation driven by the higher resolution ARM forcing of the reduced domain. The deep convective scheme is disabled in this simulation

to investigate the behavior of the shallow cumulus scheme, which is exactly intended for the kind of cloud this RACORO cumulus case represents. The two LES models are the Distributed Hydrodynamic Aerosol and Radiative Modeling Application (DHARMA) model [Ackerman *et al.* 2000; Stevens *et al.* 2002] and WRF-FASTER. The latter is built on the core of Advanced Research Version of Weather Research and Forecasting model (WRF-ARW) [Skamarock *et al.* 2008] model, but with specialized modules developed in the FASTER Project that enable the high-resolution simulations to be driven by time varying large-scale forcings. More details on the development and evaluation of WRF-FASTER as an LES model can be found in Endo *et al.* [2015]. The LES simulations are initialized and constrained by the same forcing data as for the SCAM5 runs.

Before using the LES simulations to analyze the essential parameters related to cumulus activity, we examine how well the LES models themselves simulate the cumulus clouds. The LES-simulated total cloud amounts are shown in Figure 8 with the ARSCL cloud amount (Figure 8a). (Note that the corresponding SCAM5 cumulus cloud amount is shown in Figure 6b.) The timing of the cumulus are well-captured by the LES and, compared to the shallow cumulus clouds simulated by the SCAM5, both LES models simulate more cumulus clouds. The LES cumulus clouds start earlier, penetrate higher vertically, and are more continuous in time. All of these characteristics are more comparable to the observed cumulus clouds than the SCAM5 simulations. The better agreement with observation and the consistency between the two LES simulations gives us reasonable confidence that the LES simulations can help assess the cumulus-related parameters in the SCAM5. Nevertheless, we note that the LES models in the current configuration also tend to under-produce cumulus cloud amount. The LES cloud

production is sensitive to how the simulations are forced, as investigated in *Endo et al.* [2015] and *Vogelmann et al.* [2015]. Despite this sensitivity, it should not affect the validity of this assessment, since the SCAM5 shallow cumulus convection scheme is assessed using LES simulations driven by the same forcing data.

4.1 Cumulus mass flux

Cumulus mass flux is a measure of the bulk cumulus activity. Figure 9 shows the cumulus mass flux from the SCAM5 shallow cumulus parameterization and that derived from the LES simulations. The mass fluxes from the two LES simulations are similar; however, the mass flux in SCAM5 is consistently weaker than in the LES simulations, with the SCAM5 cumulus mass flux being only about half the LES values during the most convectively active periods.

RACORO in-situ flight measurements can be used to derive an estimate of the observed cumulus mass fluxes. The RACORO campaign flew a triangular pattern at the SGP Central Facility [*Vogelmann et al.*, 2012] where each triangle is at a nearly constant altitude and the length of each leg is about 20 km. The vertical air motions at 1 Hertz, measured by a gust probe, are used to estimate the cumulus mass flux. The procedure is as follows. The flight-based values are estimated for each of the three legs to estimate the variation at a given height. The flight flew through both cloudy and clear areas at each height. The updraft mass fluxes are first calculated for the cloudy flight samples that have upward vertical velocity, $\sigma' \overline{\rho w}$, where σ' represents the fraction of updraft area among the cloudy flight samples. The domain-wide cumulus updraft area is $\sigma = A \sigma'$, where A is the domain cloud fraction. Note that the fraction of cloudy samples from all the flight samples for the leg is not necessarily equivalent to the

domain-wide cloud fraction. Here the mean cloud fraction below 4 km from ARSCL is used to represent the domain-wide cloud fraction to scale the above computed updraft mass fluxes as

$$M_c = A \sigma' \overline{\rho w}.$$

The vertical profiles of mean mass flux around the time of peak cumulus activity, between 11:30 AM to 1 PM local time, are shown for each of the three days in Figure 10 for the models and flight estimates. The flight measurements are only available at one or two narrow altitude ranges during this period and the estimates for the legs per altitude are represented by color asterisks in the plots. Particularly at the level of peak cumulus mass flux, not far from cloud base, even the LES substantially under-produced cumulus mass flux compared to those derived from the flight measurements. This appears to be consistent with the fact that LES also significantly under-produced cumulus cloud amount for this particular case and forcing data set, as previously discussed. The discrepancy between LES and flight estimates may be due to uncertainties in the forcing, the flight estimates, or from deficiencies in the LES simulations. However, there is no doubt from this comparison that, under the same forcing conditions, cumulus activity in SCAM5 is weaker, particularly for day 2 and day 3 of the simulations when the SCAM5 cumulus mass flux also peak at lower altitudes.

4.2 Planetary boundary layer turbulent kinetic energy

To explore why the cumulus activity is weaker in SCAM5, we first turn to the origin of the convective updraft as seen in the model. In the UWshcu scheme implemented in the CAM5, the convective updraft area is calculated based on how much air at the PBL top has sufficient vertical velocity to overcome convective inhibition (CIN) to reach the level of free convection.

451 Needed for this calculation is the distribution of vertical velocity at the PBL top, which is
452 assumed to have a normal distribution where the width of the distribution is determined from
453 the PBL-mean TKE (see *Bretherton et al.* [2004], and *Park and Bretherton* [2009] for more
454 details). The convective updraft area from the parameterization is the portion of the right tail
455 of the distribution that exceeds a critical vertical velocity, determined from the large-scale CIN.
456 By construct, a weaker TKE results in a narrower width of the vertical velocity distribution. For a
457 given CIN, this would lead to a smaller updraft area and a smaller mean updraft velocity
458 because less of the right tail exceeds the critical velocity. The impact on the updraft area and
459 the mean updraft velocity would give rise to smaller bulk updraft mass flux at cloud base and
460 result in weaker convective activity. The behavior of shallow cumulus activity in the model is
461 next interpreted in terms of these parameterization constructs.

462 Figure 11 shows the diagnostic TKE from the University of Washington moist turbulence
463 parameterization in the SCAM5 and that computed from the two LES simulations. Similar to
464 what was seen in the cumulus mass flux analysis, TKE in the LES simulations are comparable
465 whereas TKE in the SCAM5 is consistently weaker. As described above, this is at least partly
466 responsible for the weaker cumulus activity in the model. Besides the weaker TKE, the
467 boundary layer depth is also shallower in the SCAM5, as implied by the vertical extent of the
468 TKE field. The shallower PBL has two separate effects on low-level cloud production. First, a
469 shallower PBL would lead to a moister mixed layer (given the same rate of moisture supply
470 from the surface) that promotes relative humidity-based stratiform cloud production, forming
471 at lower altitudes. This has been clearly seen in Figure 5 that shows excessive stratiform clouds
472 throughout the day and the presence of clouds closer to the surface. Second, since the UWshcu

473 scheme is formulated to launch convective plumes from the PBL top, a shallower PBL depth
474 means that the cumulus updrafts are initiated from a lower altitude. Provided that the
475 thermodynamic profiles are the same, which largely can be ensured because the runtime
476 atmospheric profiles are relaxed toward the observations, a lower launching altitude of the
477 updraft means that a larger CIN value needs to be overcome. Just as a narrower width of the
478 vertical velocity distribution can impact cumulus activity, a lower launching level, therefore, can
479 also limit cumulus activity, leading to a smaller fractional updraft area if all else is the same.

480 Like cumulus mass flux, TKE can be diagnosed from the RACORO flights as an observational
481 reference. The 1 Hertz horizontal and vertical air motions from the RACORO flights are used to
482 derive TKE. One TKE value is computed for each leg of the flight triangle. Since the flight might
483 fly through different large-scale environments, a linear fitting is applied to each leg in order to
484 remove any trend in the background large-scale horizontal winds. TKE is computed based on
485 the detrended winds.

486 The mean TKE profiles from 11:30 AM to 1 PM local time are shown in Figure 12. The TKE in
487 the DHARMA model is slightly larger than that in WRF-FASTER below 1 km, but overall the TKE
488 in the two LES simulations are comparable and within the bounds of the flight-based
489 observations. This again supports the validity of using LES simulations as a reference to assess
490 SCAM5 performance. Evidently, the LES simulations and the observations have consistently
491 larger TKE in the PBL than does the SCAM5. There is some discrepancy between the simulated
492 TKE by the LES models and the flight-based estimates; however, none of the differences
493 contradict the fact that TKE is smaller in the SCAM5. Note that the LES-simulated TKE have

nontrivial values or even a secondary peak above the PBL, which are associated with the turbulence in the cumulus layer. In the SCAM5, the diagnostic TKE is only meaningful in the PBL.

4.3 Fractional Entrainment and Detrainment rates in the cumulus layer

Once the cumulus updraft is launched, the primary factor that controls cloud size and vertical extent is lateral mixing with the environmental air. For the bulk mass flux-based UWshcu scheme, the lateral mixing is represented by fractional entrainment and detrainment [see *Bretherton et al.*, 2004]. The lateral entrainment and detrainment can occur for the whole cloud layer in order for the bulk cloud model to mimic the presence of a nonuniform cumulus cloud ensemble [*Siebesma and Cuijpers*, 1995]. Below, we compare the fractional entrainment and detrainment rates from the SCAM5 to those derived from the LES simulations and from the RACORO flight measurements. The fractional lateral mixing rates for SCAM5 are computed in the UWshcu scheme [*Bretherton et al.*, 2004]. The LES estimates are computed by accounting for their effect on the vertical change of cumulus-core mass flux of liquid water potential temperature, following the method by *Siebesma and Cuijpers* [1995].

The profiles of mean fractional entrainment and detrainment rates from the models are shown in Figure 13, computed over 11:30 AM to 1 PM local time. The fractional detrainment rate is larger than the fractional entrainment rate for the whole cloud layer. This is consistent with the bottom-heavy structure of the mass flux profiles (Figure 10) because net detrainment causes cumulus mass flux to decrease with height. The magnitude of the LES-derived entrainment rate is comparable to that derived from the RACORO flights (Figure 3a in *Lu et al.*

[2012]). The fractional entrainment and detrainment rates in SCAM5 however are noticeably smaller than suggested by the LES.

What is puzzling is that the SCAM5 would need an even smaller fractional mixing efficiency to produce low-level clouds that are in better agreement with the observation (see section 4.4). As the detrainment rate is always larger than the entrainment rate above cloud base, a larger fractional lateral mixing efficiency would only further suppress the already weak cumulus activity. Therefore, the entrainment and detrainment parameterizations are not directly responsible for the weaker cumulus activity. If anything, the fractional entrainment and detrainment rates, which are smaller than suggested by the estimates from the flights and LES simulations, act to prevent cumulus activity from becoming even weaker. More research is needed along this direction, but is beyond the scope of this paper.

4.4 Sensitivity to model parameters and configurations

The critical role of TKE and entrainment mixing in determining shallow cumulus cloud, stratiform clouds, and deep convection through a chain of actions can be further affirmed through a suit of sensitivity experiments.

The sensitivity experiments involving key parameters controlling the UWshcu scheme are first shown in Figure 14. In the doubling TKE experiment, the PBL mean TKE is simply doubled in the calculation of the width of the distribution of turbulence vertical velocity at the PBL top. This change has no direct impact on the PBL moist turbulent processes. In the “reduced entrainment” experiment, the fractional mixing efficiency or the constant for the calculation of lateral mixing rate (i. e., the constant c in equation (A7) of *Park and Bretherton* [2009]) is

reduced by 12.5%. In the “increased max updraft fraction” experiment, the maximum core updraft fraction is increased from 10% to 15% or to the upper limit recommended by *Park and Bretherton* [2009]. The lower limit for the normalized CIN at the PBL top is changed accordingly. All three experiments are designed to increase cumulus activity and the vertical penetration depth of cumulus clouds. The results show that when the mean PBL TKE is artificially doubled, the low-level cloud biases can be reduced by a substantial amount. This is mostly realized through enhanced convective ventilation because the increased TKE only directly affect the calculations in the UWshcu scheme. Decreasing the lateral mixing efficiency in the cumulus layer or increasing the maximum allowed convective updraft area in the UWshcu scheme is even more effective in enhancing the cumulus ventilation, as seen in Figures 14c and 14d, where the persistency of low-level nighttime clouds now ceases to exist. Note, however, that the impacts are mostly from influencing the cloud production by the stratiform scheme while cloud production by the UWshcu scheme itself does not see significant increase. Particularly for the artificially doubling TKE experiment, there is no associated adjustment in the PBL parameterization and the bias in the vertical extent of the PBL turbulence remains. This is unlike the experiments shown next that have the PBL turbulence strengthen interactively along with the fully physical coupling of PBL processes and shallow cumulus convection. It is worth noting that the maximum core updraft fraction is an ad hoc parameter not dictated by LES or observation hence it is more justifiable to change than other parameters such as entrainment rate, which have stronger observational constraints. Nevertheless, these experiments provide further evidence that misrepresentation or underrepresentation of one cloud type can have important consequence on overall cloud production.

The problem of deficient PBL TKE, which is closely related to weaker cumulus activity in the SCAM5 for the RACORO cumulus case, may be alleviated if the SCAM5 is run with a different configuration. Figures 15a and b shows that the TKE simulation can be significantly improved (compared to Figure 11a) when the SCAM5 is configured with a higher vertical or horizontal resolution (hence smaller time step). For the former, each model layer below 700 mb is split into two. For the latter, the improvement with higher horizontal resolution is realized through a reduced time step allowing more time for the PBL to develop, where the time step used is one-fourth of the standard model. In both experiments, the excessive nighttime low-level clouds are substantially reduced (not shown). Cloud base height is also significantly higher in the vertical-resolution experiment. Convective cloud production from the UWshcu scheme is substantially increased for days 1 and 3 when the enhancement of PBL turbulence strength is more noticeable (Fig. 15c). This suggests that the physically based moisture turbulence scheme may be more applicable for the continental cumulus in the context of future higher-resolution climate models.

5. Summary and Discussion

Decade-long (1999-2010) Single-Column Model CAM5 simulations are first performed, driven by the long-term ARM continuous forcing at SGP site. The simulations are compared against ARM measurements in terms of the statistics of ISCCP-classification with a focus on simulated low-level clouds. The evaluation shows that SCAM5 exhibits systematic biases in occurrence frequency and cloud properties. The frequency bias is particularly large during the warm season, although the model produces mean cloud amounts not too far from the observations when

they occur. The biases in the simulated low-level cloud types result from misrepresentations of cloud processes in response to given environmental conditions.

The newly developed RACORO continental cumulus case is further used to investigate how the misrepresentation of one cloud type, specifically the underestimation of shallow cumulus clouds, may lead to excessive production of other cloud types, and to determine what factors in the shallow cumulus parameterization may be related to such undesirable behaviors.

The simulations of the shallow cumulus case by the standard SCAM5 configuration suffer from the well-known over-triggering of deep convection in early afternoon during the warm season. Even after turning off the deep convection that is not observed, the SCAM5 simulated clouds still exhibit biases of excessive and persistent low-level clouds. The shallow cumulus cloud portion of the cloud field is under-produced by the physically-based UWshcu scheme (Figure 6), which is intended for this kind of shallow cumulus cloud. The consistency among the simulations using a set of alternative forcings suggests that uncertainty in the forcing only plays a relatively minor role in this case.

With the aid of LES simulations driven by the same large-scale forcing and aircraft measurements, it is shown that the SCAM5 cumulus activity under the same prescribed environmental condition is too weak. Further diagnosis reveals that the weaker cumulus activity is related to a weaker PBL TKE in SCAM5. The weaker PBL TKE impacts the low-level cloud production in multiple ways. It directly leads to weaker cumulus updraft mass fluxes at the PBL top, and hence weaker bulk cumulus activity, because of the dependence of the UWshcu scheme on the PBL-mean TKE. Moreover, the shallower PBL depth resulting from the

weaker PBL TKE allows the buildup of moisture in the boundary layer, and hence promotes stratiform cloud production, even at the times when shallow cumuli are active. The shallower PBL depth also means that the convective updraft initiated at the PBL top has larger CIN to overcome, further reducing cumulus activity. The weaker cumulus activity in turn does not sufficiently ventilate the moisture buildup to the free troposphere, leading to excessive stratiform cloud production particularly after the temperature drops and cumulus activity subsides during nighttime.

The fractional entrainment and detrainment rates from the SCAM5 are found to be noticeably smaller than suggested by the LES simulations or flight-based estimates. The weaker fractional mixing efficiency, however, is not considered to be directly responsible for the weaker cumulus activity as measured in terms of cumulus mass flux. Sensitivity experiments show that higher temporal and vertical resolutions of the model can partially improve the simulated strength of TKE and shallow cumulus.

It is worth noting that although the focus of this study is on shallow cumulus parameterization, the successful identification of the parameterization deficiencies highlights the power of integrating SCM with LES and measurements to tackle this daunting challenge in improving fast physics parameterizations for climate models.

Acknowledgements

This research was supported by the U.S. Department of Energy Science Office of Biological and Environmental Research Program under the Earth System Modeling Program via the FASTER Project (<http://www.bnl.gov/faster>), and the Atmospheric System Research Program via DE-

620 SC0012704. Data from the DOE's SGP ARM Climate Research Facility
621 (<http://www.archive.arm.gov/>) are used in this work. His-Yen Ma and Shaocheng Xie provided
622 the RACORO period CAPT simulations.

References

- Ackerman, A.S., O.B. Toon, D.E. Stevens, A.J. Heymsfield, V. Ramanathan, and E.J. Welton, (2000), Reduction of tropical cloudiness by soot. *Science*, 288, 1042-1047, doi:10.1126/science.288.5468.1042.
- Ackerman, T. P., and G. M. Stokes (2003), The Atmospheric Radiation Measurement Program, *Phys. Today*, 56, 38–45, doi:10.1063/1.1554135.
- Bechtold, P., Chaboureau, J.-P., Beljaars, A., Betts, A. K., Köhler, M., Miller, M. and Redelsperger, J.-L. (2004), The simulation of the diurnal cycle of convective precipitation over land in a global model, *Q. J. R. Meteorol. Soc.*, 130, 3119-3137.
- Benedict, J. J. and D. A. Randall (2007), Observed Characteristics of the MJO Relative to Maximum Rainfall. *J. Atmos. Sci.*, 64, 2332–2354, doi: <http://dx.doi.org/10.1175/JAS3968.1>.
- Berg, L. K., and E. I. Kassianov (2008), Temporal variability of fair weather cumulus statistics at the ACRF SGP site, *J. Climate*, 21, 3344-3358.
- Bogenschutz, P. A., A. Gettelman, H. Morrison, V. E. Larson, D. P. Schanen, N. R. Meyer, and C. Craig (2012), Unified parameterization of the planetary boundary layer and shallow convection with a higher-order turbulence closure in the Community Atmosphere Model: Single-column experiments, *Geosci. Model. Dev.*, 5, 1407-1423.
- Bogenschutz, P. A., and S. K. Krueger (2013), A simplified PDF parameterization of subgrid-scale clouds and turbulence for cloud-resolving models, *J. Adv. Mod. Earth Syst.*, 5, 195-211, doi:10.1002/jame.20018.

643 Boucher, O., D. Randall, P. Artaxo, C. Bretherton, G. Feingold, P. Forster, V.-M. Kerminen, Y.
 644 Kondo, H. Liao, U. Lohmann, P. Rasch, S.K. Satheesh, S. Sherwood, B. Stevens and X.Y.
 645 Zhang (2013), Clouds and Aerosols. In: Climate Change 2013: The Physical Science Basis.
 646 *Contribution of Working Group I to the Fifth Assessment Report of the Intergovernmental*
 647 *Panel on Climate Change* [Stocker, T.F., D. Qin, G.-K. Plattner, M. Tignor, S.K. Allen, J.
 648 Boschung, A. Nauels, Y. Xia, V. Bex and P.M. Midgley (eds.)]. Cambridge University Press,
 649 Cambridge, United Kingdom and New York, NY, USA.

650 Bretherton, C. S., J. R. McCaa, and H. Grenier (2004), A new parameterization for shallow
 651 cumulus convection and its application to marine subtropical cloud-topped boundary layers.
 652 Part I: Description and 1D results, *Mon. Wea. Rev.*, *132*, 864-882.

653 Bretherton, Christopher S., Sungsu Park (2009), A New Moist Turbulence Parameterization in
 654 the Community Atmosphere Model, *J. Climate*, *22*, 3422–3448,
 655 doi: <http://dx.doi.org/10.1175/2008JCLI2556.1>

656 Brown, A. R., R. T. Cederwall, A. Chlond, P. G. Duynkerke, J.-C. Golaz, M. Khairoutdinov, D. C.
 657 Lewellen, A. P. Lock, M. K. MacVean, C.-H. Moeng, R. A. J. Neggers, A. P. Siebesma and B.
 658 Stevens (2002), Large-eddy simulation of the diurnal cycle of shallow cumulus convection
 659 over land, *Q. J. R. Meteorol. Soc.*, *128*, 1075-1093, doi: 10.1256/003590002320373210.

660 Cheng, A., and K.-M. Xu (2013), Evaluating Low-Cloud Simulation from an Upgraded Multiscale
 661 Modeling Framework Model. Part III: Tropical and Subtropical Cloud Transitions over the
 662 Northern Pacific, *J. Climate*, *26*, 5761–5781.

663 Clothiaux, E. E., and Coauthors (2000), Objective determination of cloud heights and radar
664 reflectivities using a combination of active remote sensors at the Atmospheric Radiation
665 Measurement Program Cloud and Radiation Test Bed (ARM CART) sites, *J. Appl. Meteor.*, *39*,
666 645-665.

667 Del Genio, A.D., Y.-H. Chen, D. Kim, and M.-S. Yao, 2012: The MJO transition from shallow to
668 deep convection in CloudSat/CALIPSO data and GISS GCM simulations. *J. Climate*, **25**, 3755-
669 3770, doi:10.1175/JCLI-D-11-00384.1.

670 Del Genio, A., and J. Wu (2010), The Role of Entrainment in the Diurnal Cycle of Continental
671 Convection, *J. Climate*, *23*, 2722-2738, doi:10.1175/2009JCLI3340.1.

672 Donner, Leo J., and Coauthors (2011): The dynamical core, physical parameterizations, and
673 basic simulation characteristics of the atmospheric component AM3 of the GFDL Global
674 Coupled Model CM3. *J. Climate*, *24*, doi:10.1175/2011JCLI3955.1.

675 Dufresne, J.-L., and S. Bony (2008), An assessment of the primary sources of spread of global
676 warming estimates from coupled atmosphere-ocean models, *J. Climate*, *21*, 5135–5144.

677 Dunn, M., K. Johnson, and M. Jensen (2011), The microbase value-added product: A baseline
678 retrieval of cloud microphysical properties. DOE/SC-ARM Technical report, DOE/SC-
679 ARM/TR-095, https://www.arm.gov/publications/tech_reports/doe-sc-arm-tr-095.pdf.

680 Endo, S. and Coauthors (2015), RACORO Continental boundary layer cloud investigations. Part II:
681 Large eddy simulations of cumulus clouds and evaluation with in-situ and ground-based
682 observations, *submitted to J. Geophys. Res.*.

683 Feng, S., and Coauthors (2015a), Development of fine-resolution analyses and expanded
684 properties of large-scale forcing, Part II: Scale-awareness and application to single-column
685 model experiments, *submitted to J. Geophys. Res.*.

686 Feng, S., and Coauthors (2015b), Development of fine-resolution analyses and expanded
687 properties of large-scale forcing, Part III: Hydrometeor forcing and application to single-
688 column model experiments, *submitted to J. Geophys. Res.*.

689 Gettelman, A., J. E. Kay, and K. M. Shell (2012), The evolution of climate sensitivity and climate
690 feedbacks in the community atmosphere model, *J. Climate*, *25*, 1453-1469,
691 doi:10.1175/JCLI-D-11-00197.1.

692 Guichard, F., and Coauthors (2004), Modelling the diurnal cycle of deep precipitating
693 convection over land with cloud-resolving models and single-column models, *Quart. J. Roy.*
694 *Meteor. Soc.*, *130*, 3139-3192.

695 Hartmann, Dennis L., Maureen E. Ockert-Bell, Marc L. Michelsen, 1992: The Effect of Cloud Type
696 on Earth's Energy Balance: Global Analysis. *J. Climate*, *5*, 1281–1304.
697 doi: <http://dx.doi.org/10.1175/1520-0442>.

698 Iacono, M. J., J. S. Delamere, E. J. Mlawer, M. W. Shephard, S. A. Clough, and W. D. Collins
699 (2008), Radiative forcing by long-lived greenhouse gases: Calculations with the ARE
700 radiative transfer model, *J. Geophys. Res.*, *113*, D13103, doi:10.1029/2008JD009944.

701 Johnson, Richard H., Thomas M. Rickenbach, Steven A. Rutledge, Paul E. Ciesielski, Wayne H.
 702 Schubert (1999), Trimodal Characteristics of Tropical Convection. *J. Climate*, 12, 2397–2418.
 703 doi: <http://dx.doi.org/10.1175/1520-0442>.

704 Kay, J. E., and Coauthors (2012), Exposing global cloud biases in the Community Atmosphere
 705 Model (CAM) using satellite observations and their corresponding instrument simulators, *J.*
 706 *Climate*, 25, 5190-5207.

707 Kennedy, A. D., X. Dong, B. Xi, P. Minnis, A. D. Del Genio, A. B. Wolf, and M. M. Khaiyer (2010),
 708 Evaluation of the NASA GISS Single Column Model simulated clouds using combined surface
 709 and satellite observations, *J. Climate*, 23, 5175-5192.

710 Klein, S., and and C. Jakob (1999), Validation and sensitivities of frontal clouds simulated by the
 711 ECMWF model. *Mon. Wea. Rev.*, 127, 2514-2531.

712 Larson, V. E., and J.-C. Golaz (2005), Using probability density functions to derive consistent
 713 closure relationships among higher-order moments, *Mon. Weather Rev.*, 133, 1023-1042.

714 Li, Z., S. Feng, Y. Liu, W. Lin, M. Zhang, T. Toto, A. M. Vogelmann, and S. Endo (2015),
 715 Development of fine-resolution analyses and expanded large-scale forcing properties, Part I:
 716 Methodology and Evaluation, *submitted to J. Geophys. Res.*.

717 Lenderink, G., and Coauthors (2004), The diurnal cycle of shallow cumulus clouds over land: A
 718 single-column model intercomparison study. *Quart. J. Roy. Meteor. Soc.*, 130, 3339-3364.

719 Lu, C., Y. Liu, S. Niu, and A. M. Vogelmann (2012), Lateral entrainment rate in shallow cumuli:
 720 Dependence on dry air sources and probability density functions, *Geophys. Res. Lett.*, 39,
 721 L20812, doi:10.1029/2012GL053646.

722 Mather, J. H., and J. W. Voyles (2013), The Arm Climate Research Facility: A Review of Structure
 723 and Capabilities, *Bull. Amer. Meteor. Soc.*, *94*, 377–392, doi:
 724 <http://dx.doi.org/10.1175/BAMS-D-11-00218.1>

725 Medeiros, B., B. Stevens, I. M. Held, M. Zhao, D. L. Williamson, J. G. Olson, and C. S. Bretherton
 726 (2008), Aquaplanets, climate sensitivity, and low clouds, *J. Climate*, *21*, 4974-4991.

727 Morrison, H., and A. Gettelman (2008), A new two-moment bulk stratiform cloud microphysics
 728 scheme in the Community Atmospheric Model (CAM3), Part I: Description and numerical
 729 tests, *J. Climate*, *21*, 3845-3862.

730 Neale, R. B., J. H. Richter, and M. Jochum (2008), The impact of convection on ENSO: from a
 731 delayed oscillator to a series of events, *J. Climate*, *21*, 5904-5924.

732 Neale, R. B., C.-C. Chen, A. Gettelman, P. H. Lauritzen, S. Park, D. L. Williamson, A. J. Conley, R.
 733 Garcia, D. Kinnison, J.-F. Lamarque, D. Marsh, M. Mills, A. K. Smith, S. Tilmes, F. Vitt, H.
 734 Morrison, P. Cameron-Smith, W. D. Collins, M. J. Iacono, R. C. Easter, S. J. Ghan, X. Liu, P. J.
 735 Rasch, and M. A. Taylor (2012), Description of the NCAR Community Atmosphere Model
 736 (CAM 5.0), *NCAR Technical Note, NCAR/TN-486+STR*.

737 Neale, R. B., J. H. Richter, A. J. Conley, S. Park, P. H. Lauritzen, A. Gettelman, D. L. Williamson, P.
 738 J. Rasch, S. J. Vavrus, M. A. Taylor, W. D. Collins, M. Zhang, S.-J. Lin, 2010: Description of the
 739 NCAR Community Atmosphere Model (CAM4.0), *NCAR Technical Note, NCAR/TN-485+STR*.

740 Neggers, R. A. J., A. P. Siebesma, G. Lenderink, and A. A. M. Holtslag (2004), An evaluation of
 741 mass flux closures for diurnal cycles of shallow cumulus, *Mon. Wea. Rev.*, *132*, 2525-2538.

742 Norris, J. R., 1998: Low cloud type over the ocean from surface observations. Part I: relationship
 743 to surface meteorology and the vertical distribution of temperature and moisture. *J.*
 744 *Climate*, 11, 369-382.

745 Park, S., and C. S. Bretherton (2009), The University of Washington shallow convection and
 746 moist turbulence schemes and their impact on climate simulations with the community
 747 atmosphere model, *J. Climate.*, 22, 3449-3469.

748 Park, S., C. S. Bretherton, and P. J. Rasch (2014), Integrating cloud processes in the community
 749 atmosphere model, version 5, *J. Climate.*, 27, 6821-6856.

750 Randall, D. A., K.-M. Xu, R. J. C. Somerville, and S. Iacobellis (1996), Single-column models and
 751 cloud ensemble models as links between observations and climate models, *J. Climate*, 9,
 752 1683-1697.

753 Randall, D. A., et al. (2007), Climate models and their evaluation. In: Climate Change 2007: The
 754 Physical Science Basis. *Contribution of Working Group I to the Fourth Assessment Report of*
 755 *the Intergovernmental Panel on Climate Change* [Solomon, S., D. Qin, M. Manning, Z. Chen,
 756 M. Marquis, K. B. Averyt, M. Tignor and H. L. Miller (eds.)] Cambridge University Press,
 757 Cambridge, United Kingdom and New York, NY, USA, pp. 589–662.

758 Rossow, W. B., A. W. Walker, D.E. Beuschel, and M. D. Roiter (1996), International Satellite
 759 Cloud Climatology Project (ISCCP) Documentation of New Cloud Datasets, *WMO/TD-No.*
 760 737, World Meteorological Organization, 115 pp.

761 Skamarock, W. C., and Coauthors (2008), A description of the Advanced Research WRF version
 762 3. NCAR Tech. Note NCAR/TN-475+STR, 113 pp.

763 Sherwood, S. C., S. Bony, and J.-L. Dufresne (2014), Spread in model climate sensitivity traced to
 764 atmospheric convective mixing. *Nature*, 505, 37-42, doi:10.1038/nature12829.

765 Siebesma, A. P. and J. W. M. Cuijpers (1995), Evaluation of parametric assumptions for
 766 shallow cumulus convection, *J. Atmos. Sci.*, 52, 650-666.

767 Siebesma, A. P. (1998), Shallow Cumulus Convection , in: Buoyant Convection in Geophysical
 768 Flows. Pforzheim, Germany, 17-27 March NATO Advanced Study Institute. edited by
 769 E.J. Plate, E.E. Fedorovich, X.V. Viegas and J.C. Wyngaard p.441-486, Kluwer.

770 Siebesma, A. P., P. M. M. Soares, and J. Teixeira (2007), A combined Eddy Diffusivity Mass Flux
 771 approach for the convective boundary layer, *J. Atmos. Sci.*, 64, 1230-1248.

772 Song, H., and Coauthors (2013), Evaluation of precipitation simulated by seven SCMs against
 773 the ARM observations at the SGP site, *J. Climate*, 26, 5467–5492.

774 Stevens, D. E., A. S. Ackerman, and C. S. Bretherton (2002), Effects of domain size and numerical
 775 resolution on the simulation of shallow cumulus convection. *J. Atmos. Sci.*, 59, 3285–3301.

776 Stokes, G. M., and S. E. Schwartz (1994), The Atmospheric Radiation Measurement (ARM)
 777 program: Programmatic background and design of the cloud and radiation testbed, *Bull.*
 778 *Amer. Meteor. Soc.*, 75, 1201-1221.

779 Suselj, K., J. Teixeira, and G. Matheou (2012), EDMF and shallow cumulus boundary layer: An
 780 updraft pdf multiple mass-flux scheme. *J. Atmos. Sci.*, 69, 1513-1533.

781 Tiedtke, M., W. A. Heckley, and J. Slingo (1988), Tropical forecasting at ECMWF: The influence
 782 of physical parameterization on the mean structure of forecasts and analyses, *Q. J. R.*
 783 *Meteorol. Soc.*, 114, 639-664.

784 Vogelmann, A. M., G. M. McFarquhar, J. A. Ogren, D. D. Turner, J. M. Comstock, G. Feingold, C.
 785 N. Long, H. H. Johnson, A. Bucholtz, D. R. Collins, G. S. Diskin, H. Gerber, R. P. Lawson, R. K.
 786 Woods, E. Andrews, H.-J. Yang, J. C. Chiu, D. Hartsock, J. M. Hubbe, C. Lo, A. Marshak, J. W.
 787 Monroe, S. A. McFarlane, B. Schmid, J. M. Tomlinson, and T. Toto (2012), RACORO
 788 extended-term aircraft observations of boundary layer clouds. *Bull. Amer. Meteor. Soc.*, *93*,
 789 861-878.

790 Vogelmann, A. M., and coauthors (2015), RACORO Continental boundary layer cloud
 791 investigations. Part I: Case study generation and ensemble large-scale forcings, *submitted*
 792 *to J. Geophys. Res.*.

793 Walters, D. N., and Coauthors (2011), The Met Office Unified Model global atmosphere 3.0/3.1
 794 and JULES global land 3.0/3.1 configurations, *Geosci. Model Dev.*, *4*, 919-941,
 795 doi:10.5194/gmd-4-919-2011.

796 Warren, S.G., C.J. Hahn, J. London, R.M Chervin and R.L. Jenne (1986), Global Distribution of
 797 Total Cloud Cover and Cloud Type Amounts over Land. *NCAR Technical Note*, TN-273+STR,
 798 Boulder, CO, 29 pp. + 200 maps (also DOE/ER/60085-H1)

799 Warren, S.G., C.J. Hahn, J. London, R.M Chervin and R.L. Jenne (1988), Global Distribution of
 800 Total Cloud Cover and Cloud Type Amounts over the Ocean. *NCAR Technical Note*, TN-
 801 317+STR, Boulder, CO, 42 pp. + 170 maps (also DOE/ER-0406).

802 Wu, Z. (2003), A shallow CISK, deep equilibrium mechanism for the interaction between large-
 803 scale convection and large-scale circulations in the tropics, *J. Atmos., Sci.*, *60*, 377-392.

804 Xie, S., R. T. Cederwall, and M. Zhang (2004), Developing long-term single-column model/cloud
805 system-resolving model forcing data using numerical weather prediction products
806 constrained by surface and top of atmosphere observations, *J. Geophys. Res.*, *109*, D01104,
807 doi: 10.1029/2003JD004045.

808 Xu, K.-M., and A. Cheng (2013), Evaluating Low-Cloud Simulation from an Upgraded Multiscale
809 Modeling Framework Model. Part I: Sensitivity to Spatial Resolution and Climatology, *J.*
810 *Climate*, *26*, 5717–5740.

811 Zhang, G. J., and N. A. McFarlane (1995), Sensitivity of climate simulations to the
812 parameterization of cumulus convection in the Canadian Climate Centre General
813 Circulation Model, *Atmos.-Ocean*, *33*(3), 407-446.

814 Zhang, M., and Coauthors (2013), CGILS: Results from the first phase of an international project
815 to understand the physical mechanisms of low cloud feedbacks in general circulation
816 models, *J. Adv. Mod. Earth Syst.*, doi:10.1002/2013MS000246.

817 Zhang, Y., and S. A. Klein (2010), Mechanism affecting the transition from shallow to deep
818 convection over land: Inferences from observations of the diurnal cycle collected at the
819 ARM Southern Great Plain site, *J. Atmos. Sci.*, *67*, 2943-2959.

820 Zhang, G. J., and N. A. McFarlane (1995), Sensitivity of climate simulations to the
821 parameterization of cumulus convection in the Canadian Climate Centre General
822 Circulation Model, *Atmos.-Ocean*, *33*(3), 407-446.

823 Zhu, P., and B. Albrecht (2002), A theoretical and observational analysis on the formation of
824 fair-weather cumulus, *J. Atmos. Sci.*, *59*, 1983-2005.

825 Zhu, P., and B. Albrecht (2003), Large eddy simulations of continental shallow cumulus
826 convection, *J. Geophys. Res.*, *108*, D15, doi:10.1029/2002JD003119.

827 **Figure Captions**

828 Figure 1. Seasonal variation of (a) upper panel, frequency occurrence of low clouds with less
829 than 10% overlying upper-level cloud coverage, and (b) lower panel, mean cloud amounts when
830 low-level clouds are present.

831 Figure 2. Warm season (May-August) relative occurrence frequencies of cloud types as a
832 function of cloud-top pressure and optical depth for low-level cloudy conditions that have less
833 than 10% overlying clouds for (a) Microbase, and (b) SCAM5. The gray two letter symbols
834 denote canonical cloud types for the corresponding bins of optical depth and cloud-top
835 pressure. The relative frequency of each cloud type is calculated based on its occurrence
836 regardless of its cloud amount.

837 Figure 3. As for figure 2 except for means where, unlike the previous figure for relative
838 frequency, cloud amount for each type is explicitly accounted for to produce the mean
839 histogram..

840 Figure 4. Time-height distribution of hourly mean cloud fraction from local solar time 6 AM May
841 22 through 6 PM May 24 2009 from (a) ARSCL, and (b) – (g) SCAM5 simulations driven with
842 different forcings as indicated in each panel. The right panels are for simulations with forcings
843 for the reduced domain (150km) and the left use the standard domain (300 km). All
844 simulations are initialized with the SGP central facility sounding near local time 6 AM May 22.

845 Figure 5. Same as Figure 4 except for SCAM5 simulations with the model's deep convection
846 scheme turned off.

847 Figure 6. Same as Figure 5 except for convective cloud fraction produced by the model's
848 shallow cumulus convection scheme.

849 Figure 7. Relative humidity from the ARM forcing for the reduced domain (a), and SCAM5
850 simulations with deep convection (b) and without deep convection (c).

851 Figure 8. Time-height distribution of clouds from ARSCL observations, and LES simulations by
852 DHARMA and WRF-FASTER. The ARSCL cloud is the same as in Fig. 4a except with a reduced
853 height range. Fig. 6b shows the corresponding SCAM5-simulated shallow cumulus clouds.

854 Figure 9. Cumulus mass flux from SCAM5, and LES simulations by DHARMA and WRF-FASTER.

855 Figure 10. Mean cumulus updraft mass flux between 11: 30 AM and 1 PM local time for day
856 1(left), day 2 (middle), and day 3 (right). The asterisks are RACORO-flight derived values, where
857 colors indicate different flight legs (see text for details).

858 Figure 11. Turbulent kinetic energy from SCAM5, DHARMA and WRF-FASTER.

859 Figure 12. As in Figure 10 except for turbulent kinetic energy (TKE).

860 Figure 13. Mean fractional entrainment (blue) and detrainment (red) rates between 11:30 AM
861 and 1 PM local time from SCAM5 (top), DHARMA (middle), and WRF-FASTER (bottom). The
862 columns from left to right are for days 1, 2, and 3, respectively.

863 Figure 14. Time-height distribution of SCAM5 simulated clouds in response to parameter
864 changes that affect the shallow cumulus simulation. Note that reduction in entrainment
865 efficiency also affects detrainment rate.

866 Figure 15. TKE from SCAM5 simulations with (a) smaller time step and (b) increased vertical
867 resolution, and convective cloud fraction associated with the simulation in (a). See text for
868 details.

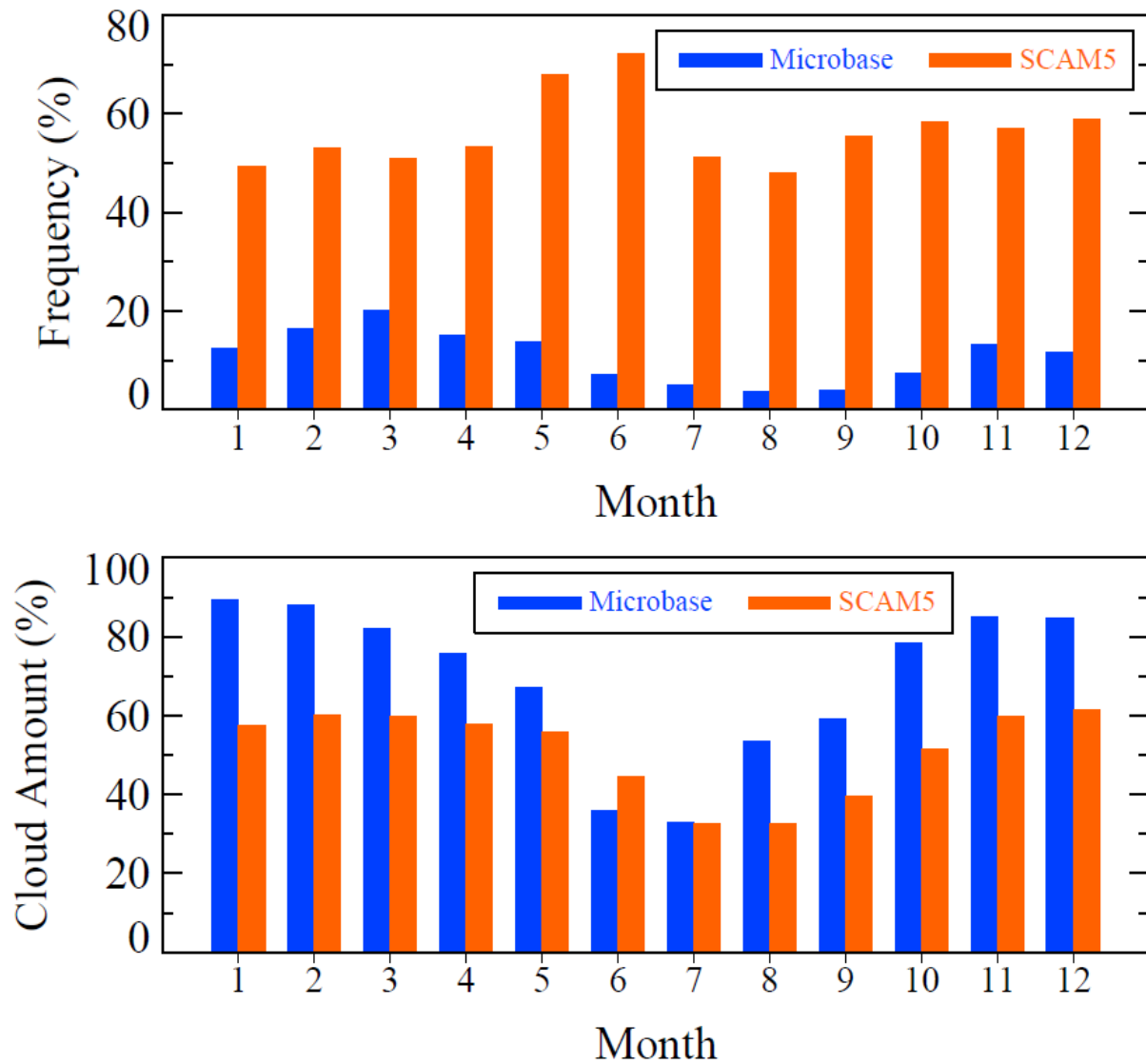


Figure 1. Seasonal variation of (a) upper panel, frequency of occurrence of low clouds with less than 10% overlying upper-level cloud coverage, and (b) lower panel, mean cloud amounts when low-level clouds are present.

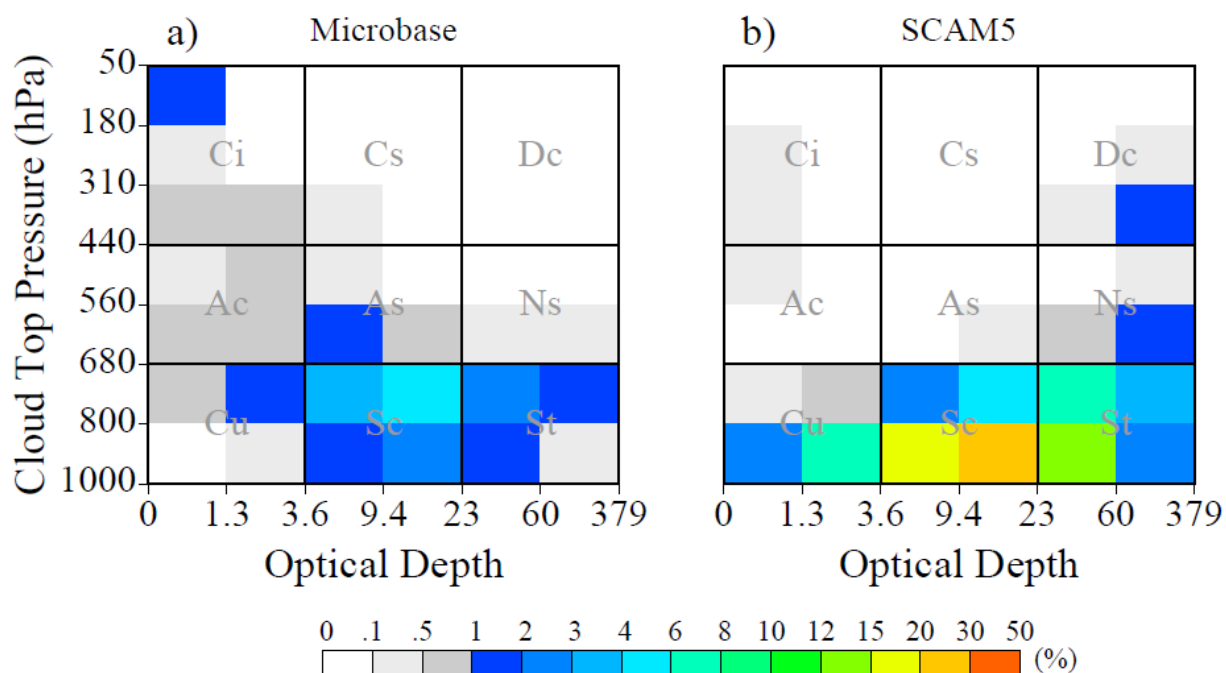


Figure 2. Warm season (May-August) relative occurrence frequencies of cloud types as a function of cloud-top pressure and optical depth for low-level cloudy conditions that have less than 10% overlying clouds for (a) Microbase, and (b) SCAM5. The gray two letter symbols denote canonical cloud types for the corresponding bins of optical depth and cloud-top pressure. The relative frequency of each cloud type is calculated based on its occurrence regardless of its cloud amount.

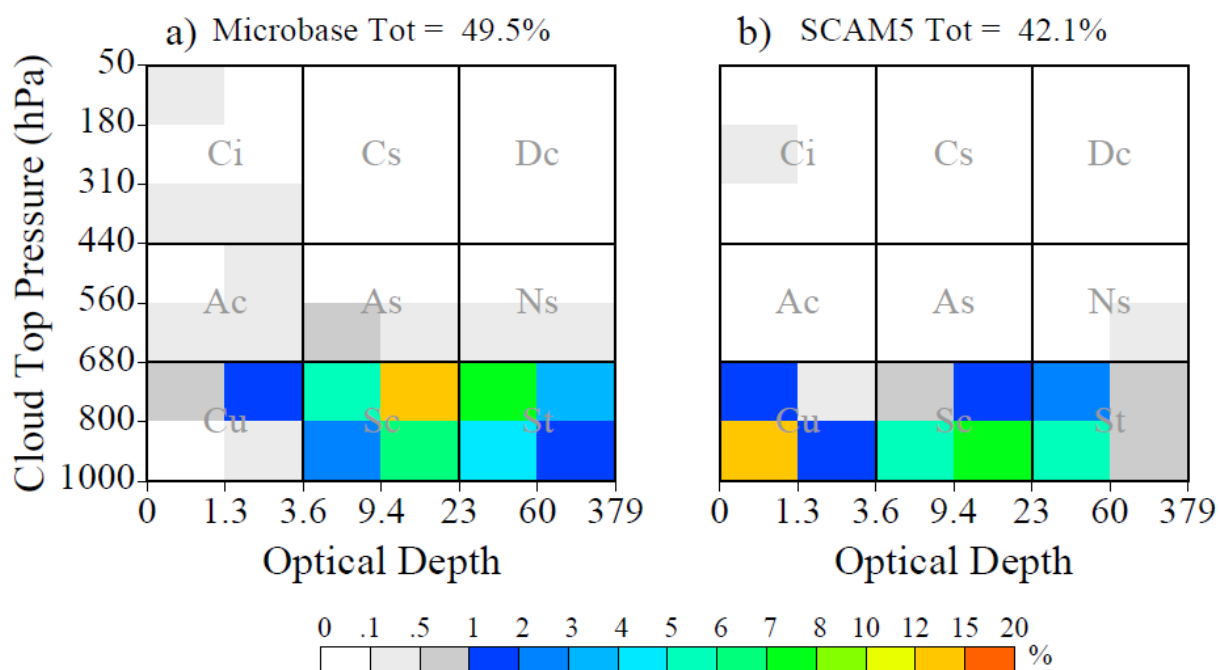


Figure 3. As for figure 2 except for means where, unlike the previous figure for relative frequency, cloud amount for each type is explicitly accounted for to produce the mean histogram.

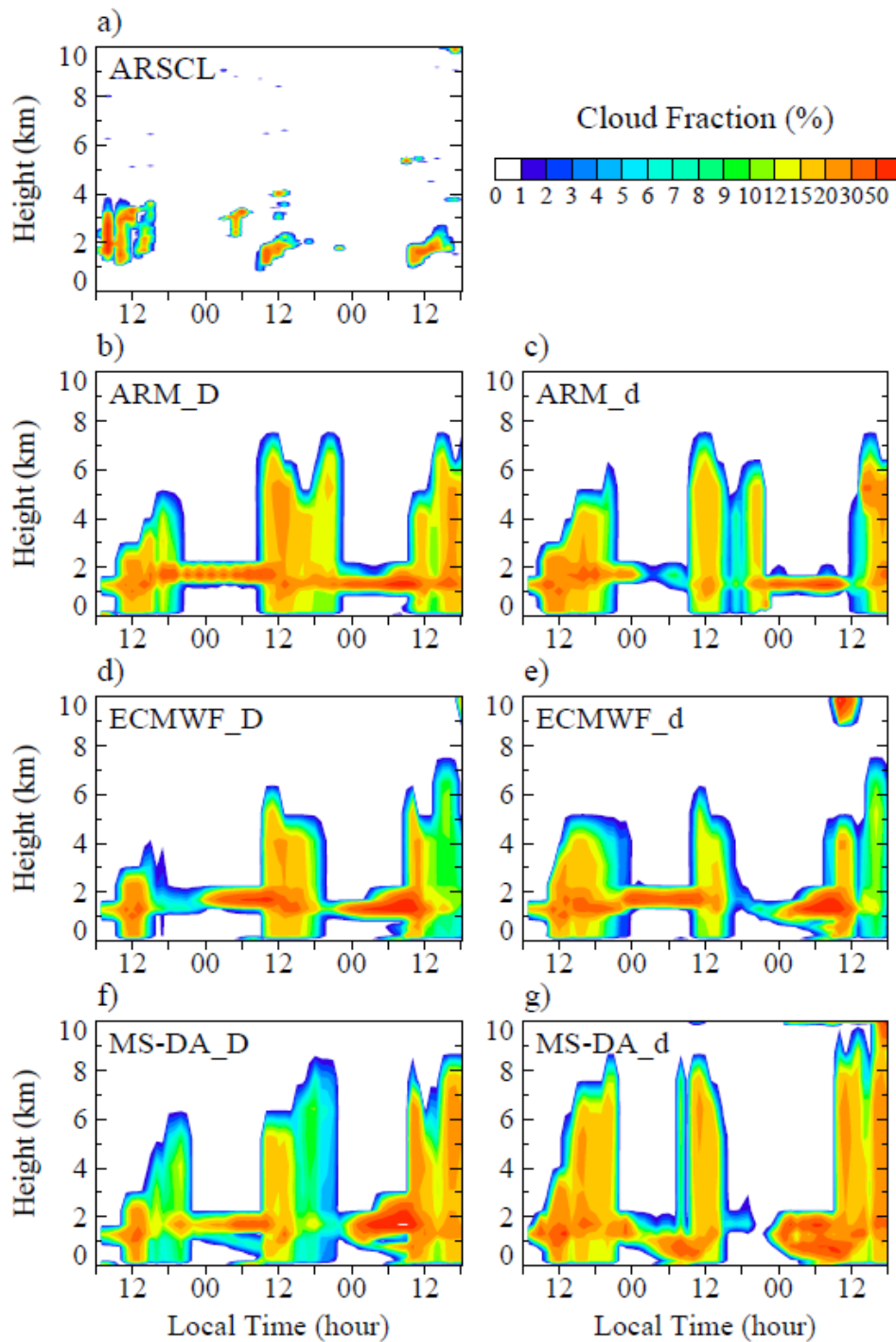


Figure 4. Time-height distribution of hourly mean cloud fraction from local solar time 6 AM May 22 through 6 PM May 24, 2009 from (a) ARSCL, and (b) – (g) SCAM5 simulations driven with different forcings as indicated in each panel. The right panels are for simulations with forcings for the reduced domain (150 km) and the left panel use the standard domain (300 km). All simulations are initialized with the SGP central facility sounding near local time 6 AM May 22.

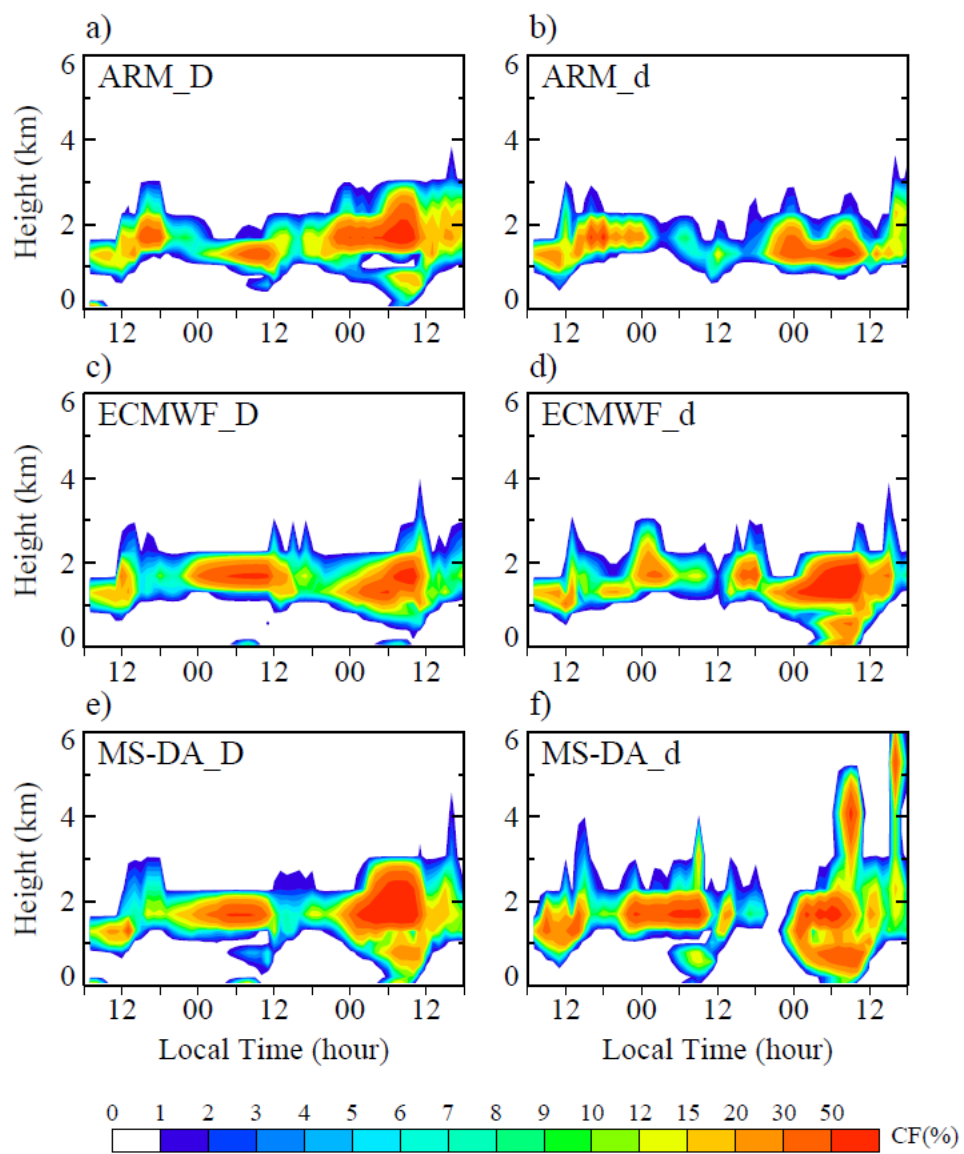


Figure 5. Same as Figure 4 except for SCAM5 simulations with the model's deep convection scheme turned off.

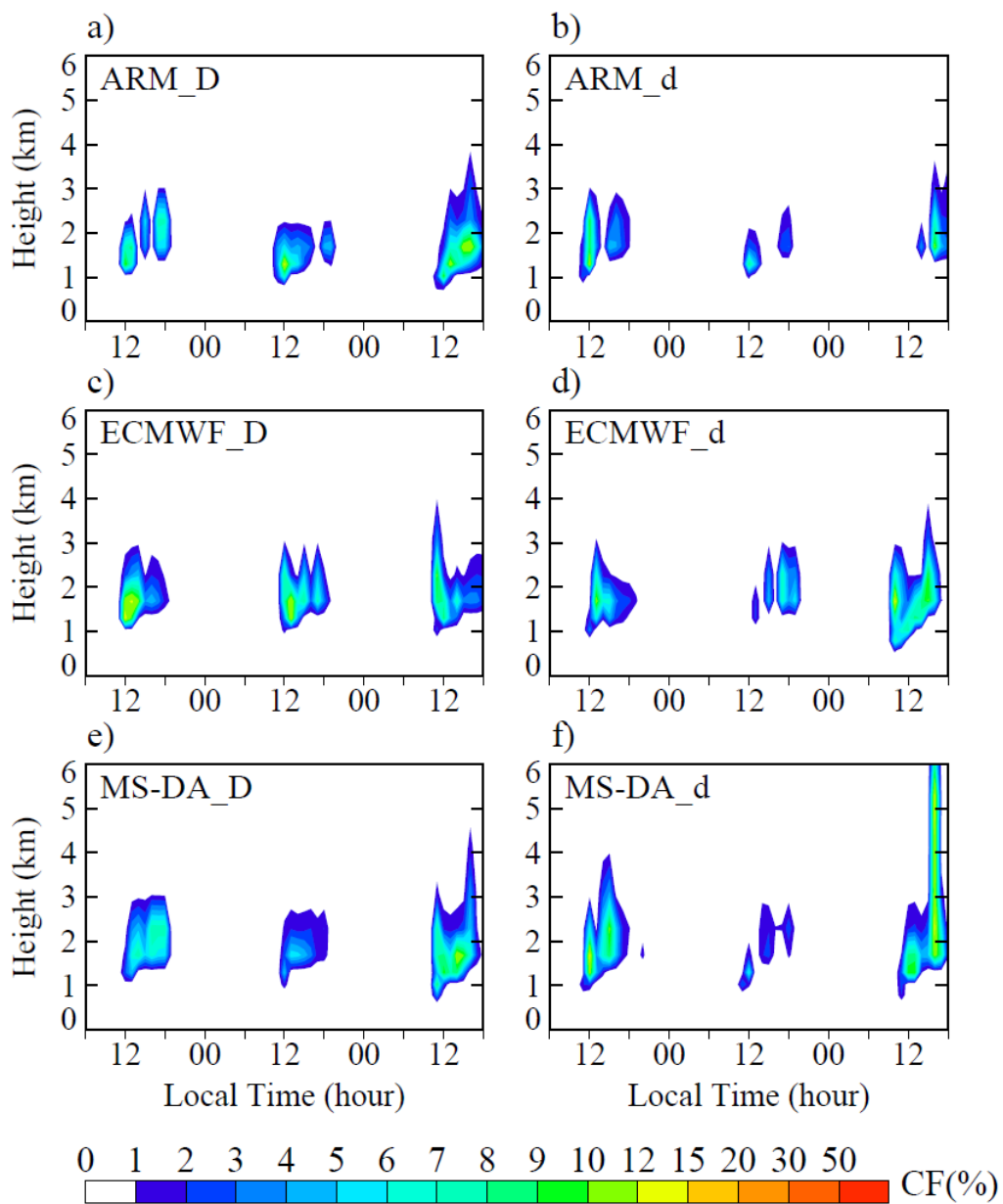


Figure 6. Same as Figure 5 except for convective cloud fraction produced by the model's shallow cumulus convection scheme.

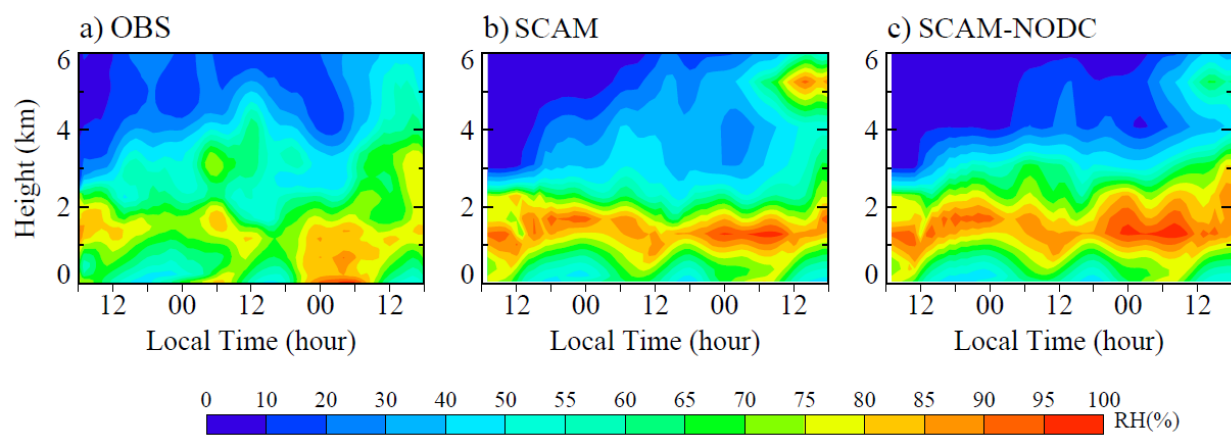


Figure 7. Relative humidity from the ARM forcing for the reduced domain (a), and SCAM5 simulations with deep convection (b) and without deep convection (c).

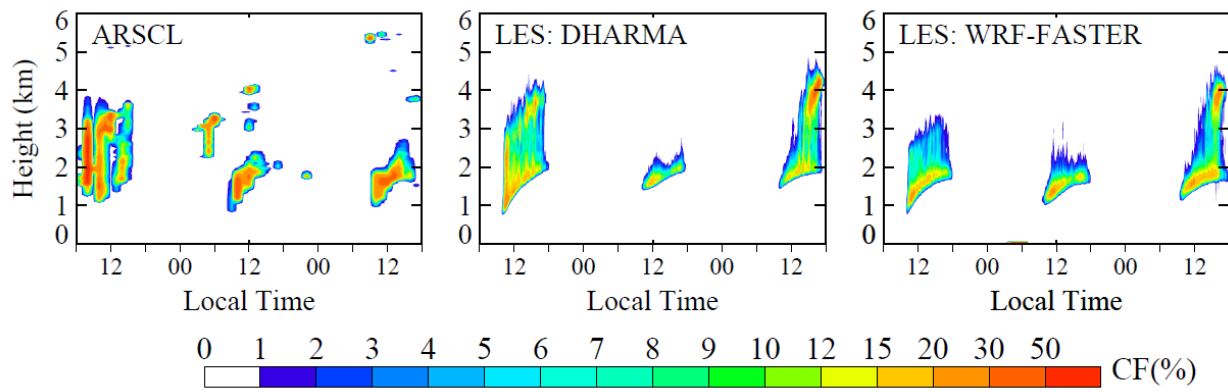


Figure 8. Time-height distribution of clouds from ARSCL observations, and LES simulations by DHARMA and WRF-FASTER. The ARSCL cloud is the same as in Fig. 4a except with a reduced height range. Fig. 6b shows the corresponding SCAM5-simulated shallow cumulus clouds.

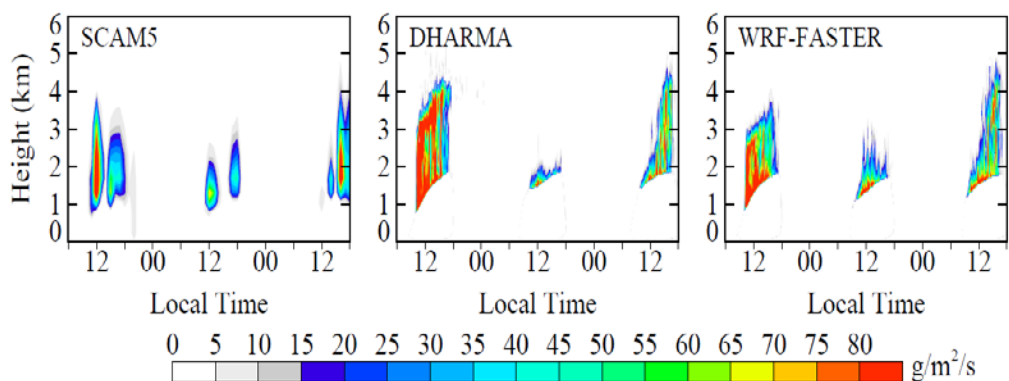


Figure 9. Cumulus mass flux from the SCAM5, and LES simulations by DHARMA and WRF-FASTER.

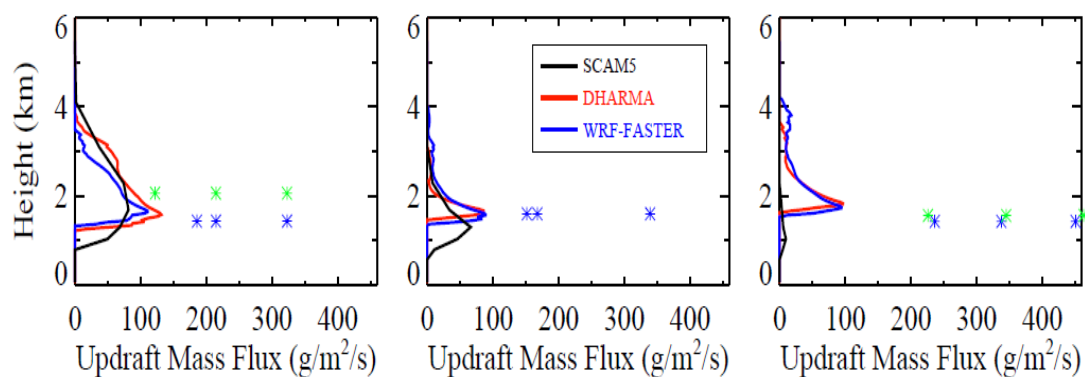


Figure 10. Mean cumulus updraft mass flux between 11: 30 AM and 1 PM local time for day 1(left), day 2 (middle), and day 3 (right). The asterisks are RACORO-flight derived values, where colors indicate different flight legs (see text for details).

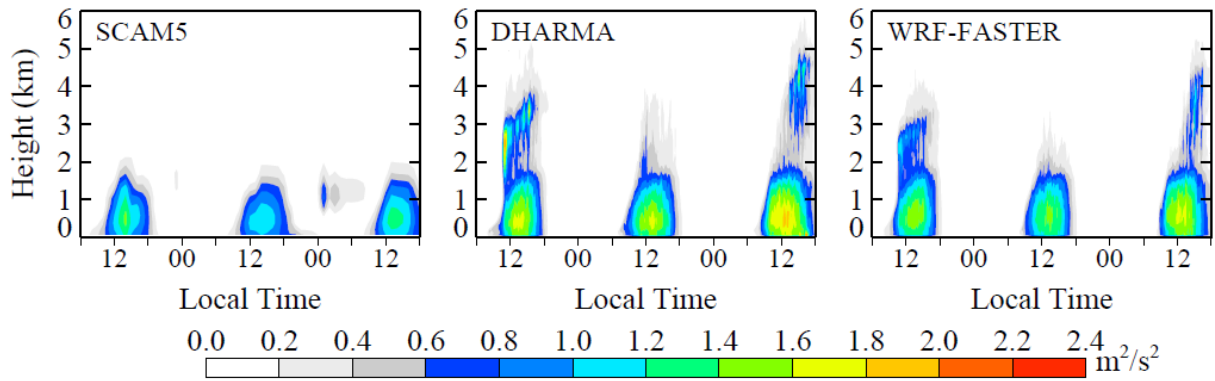


Figure 11. Turbulent kinetic energy from SCAM5, DHARMA and WRF-FASTER.

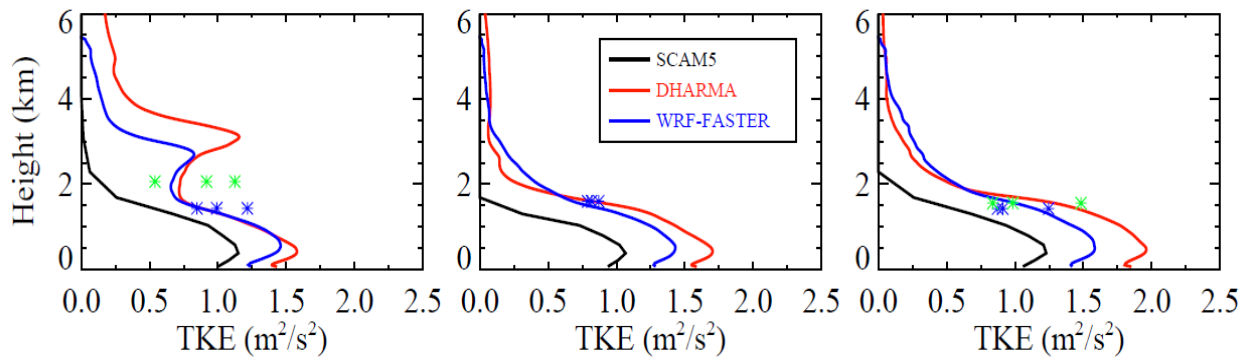


Figure 12. As in Figure 10 except for turbulent kinetic energy (TKE).

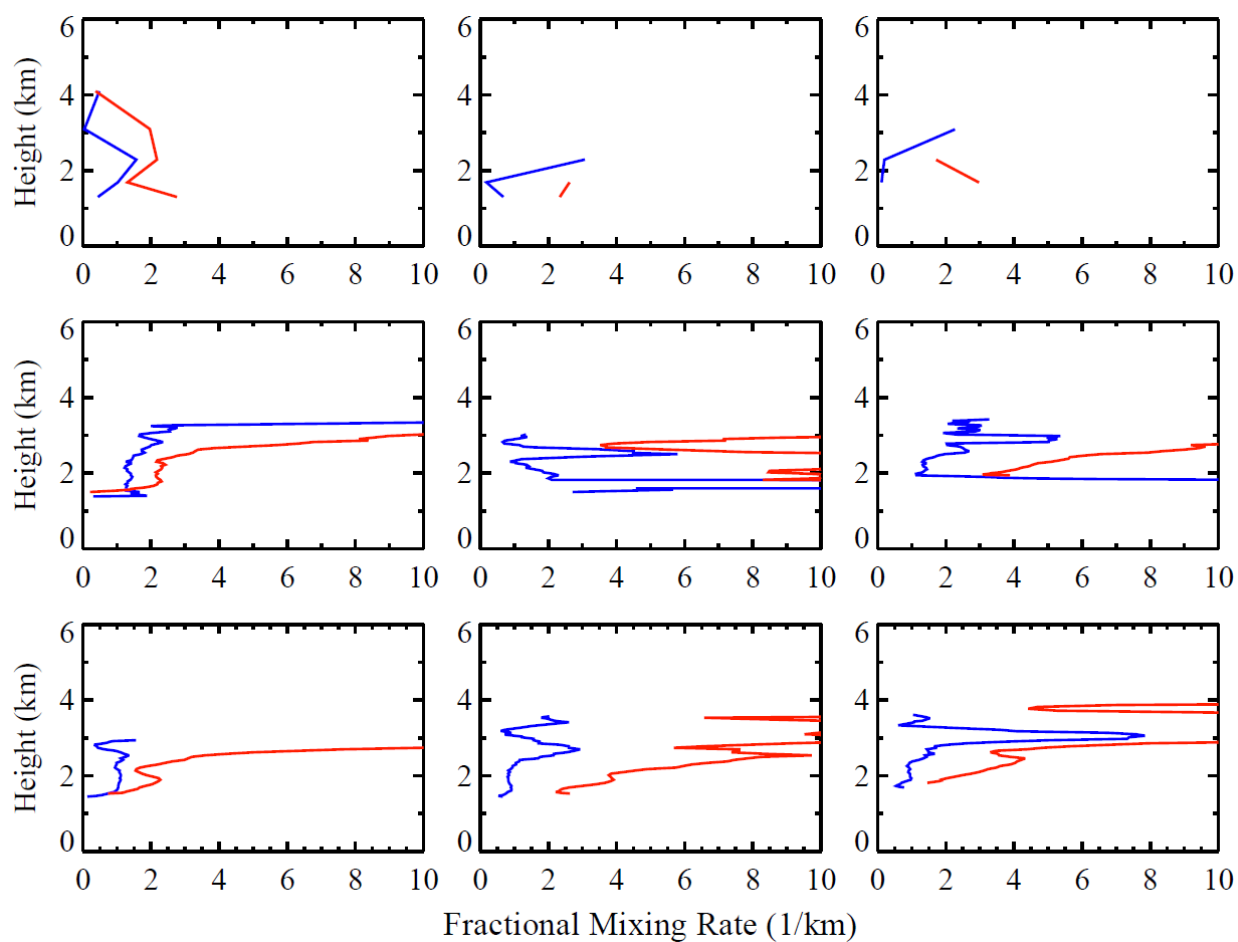


Figure 13. Mean fractional entrainment (blue) and detrainment (red) rates between 11:30 AM and 1 PM local time from SCAM5 (top), DHARMA (middle), and WRF-FASTER (bottom). The columns from left to right are for days 1, 2, and 3, respectively.

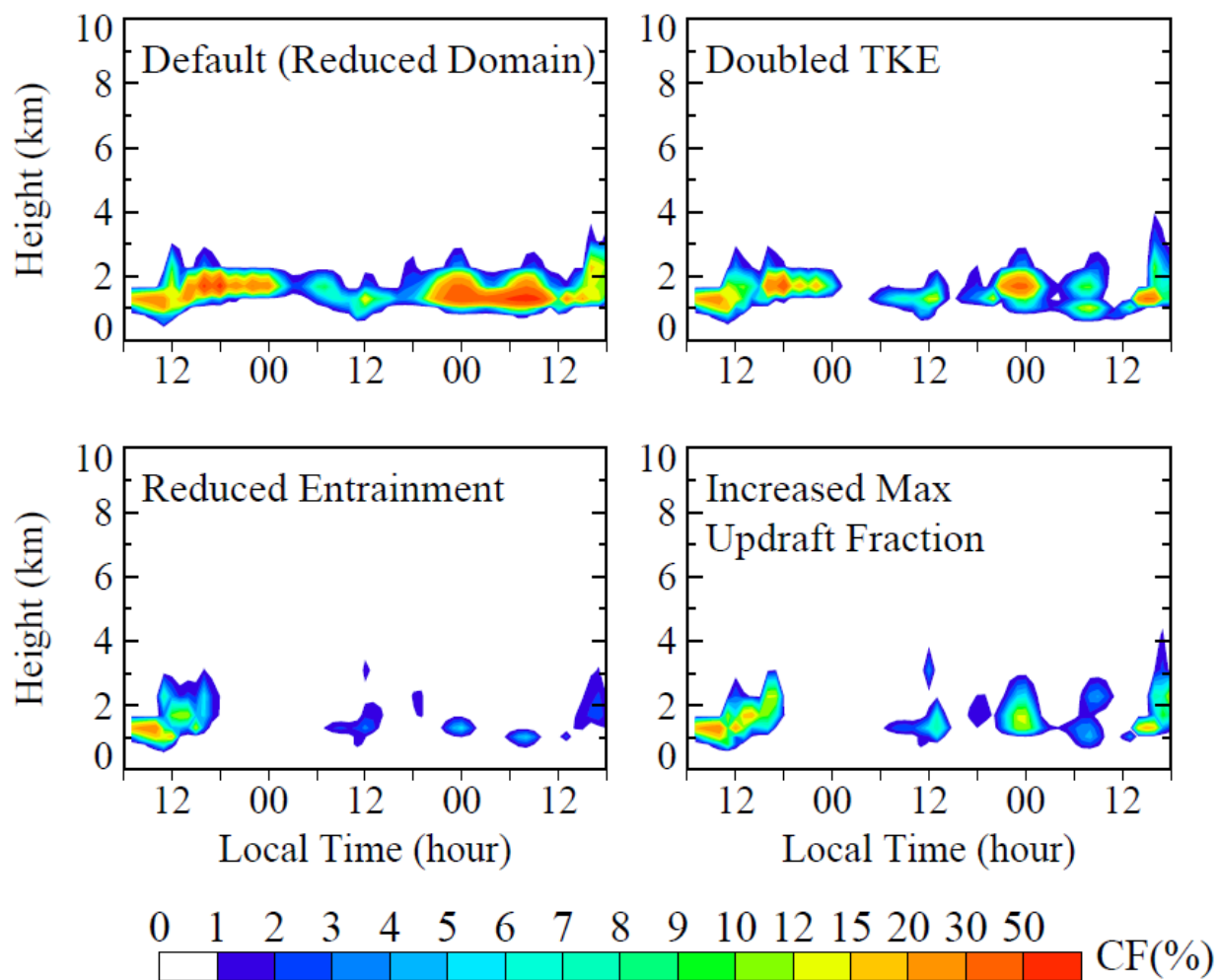


Figure 14. Time-height distribution of SCAM5 simulated clouds in response to parameter changes that affect the shallow cumulus simulation. Note that reduction in entrainment efficiency also affects detrainment rate.

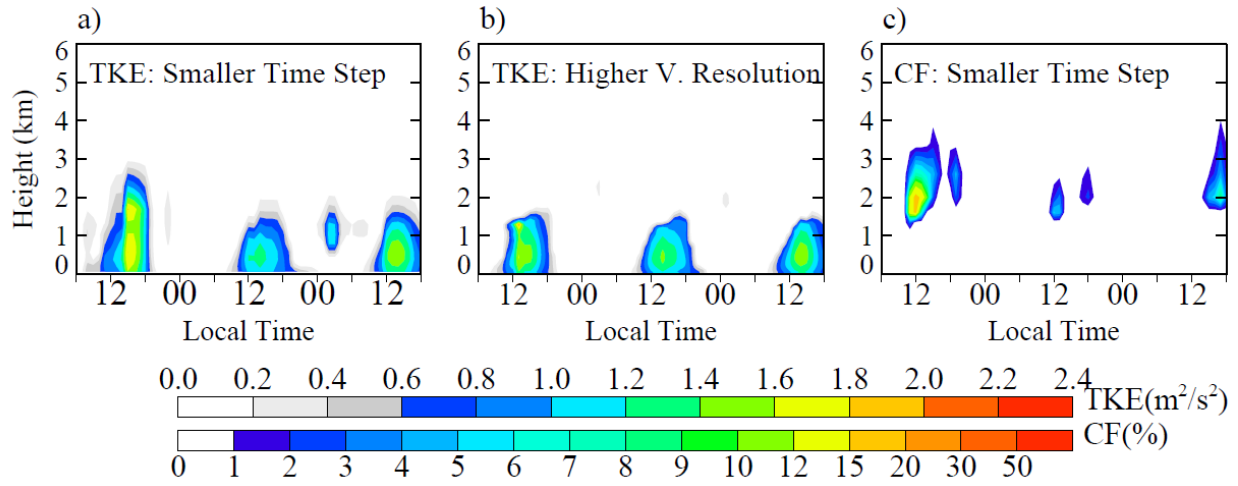


Figure 15. TKE from SCAM5 simulations with (a) smaller time step and (b) increased vertical resolution, and convective cloud fraction associated with the simulation in (a). See text for details.